This is a Just Accepted version, keep updated with https://doi.org/10.26599/OCEAN.2026.9470018
*OCEAN* **2026, 2, 9470018**

**Article type:** Original Research
https://doi.org/10.26599/OCEAN.2026.9470018

# Dimensional analysis on piston-mode narrow-gap resonances of two fixed side-by-side barges under Stokes waves

Yunfeng Ding[1], Qicai Niu[2], Jens Honoré Walther[3], Hua-Dong Yao[1], Yanlin Shao[3,*]

[1]*Marine Technology, Mechanics and Maritime Sciences, Chalmers University of Technology, Göteborg, 412 96, Sweden*

[2]*Kyushu University, Fukuoka 816-8580, Japan*

[3]*Department of Civil and Mechanical Engineering, Technical University of Denmark, Kongens Lyngby, DK-2800, Denmark*

***Corresponding author(s):** Yanlin Shao**,** yshao@dtu.dk

**Received:** November 1, 2025 **/ Revised:** December 18, 2025 **/ Accepted:** January 4, 2026



## ABSTRACT

A dimensional analysis is presented for piston-mode resonant fluid response between two identical, fixed, side-by-side barges subjected to Stokes waves. Based on a simplified physical model, the key parameters governing the resonant response of the water column confined in the gap are identified. For a two-dimensional deep-water, wave-only configuration, wave steepness and draft-to-beam ratio are found to be the two principal non-dimensional parameters. Numerical simulations are performed in a fully nonlinear wave tank over a range of these two parameters. As the draft-to-beam ratio increases, the non-dimensional resonant wave amplitude within the gap rises monotonically and then remains almost constant beyond a certain value. For the considered wave steepness, the resonant response tends to be inversely proportional to the wave steepness owing to the quadratic nature of the damping. To this end, a physics-based empirical formula is subsequently derived to provide a convenient tool for rapid estimation of resonant fluid response in the considered configuration. Although the accuracy of this empirical formula depends on the ranges of the governing parameters covered in the numerical simulations, it demonstrates fairly satisfactory agreement with other existing experimental and numerical results within similar parameter ranges. It is expected that the present approach can be extended to three-dimensional gap resonance problems between two barges where other modes of resonance are predominant.

**KEYWORDS**

Piston-mode resonant fluid response; Dimensional analysis; Draft-to-beam ratio; Wave steepness; Computational Fluid Dynamics

## 1 Introduction

Floating Production Storage and Offloading (FPSO) units and Floating Liquefied Natural Gas (FLNG) facilities have become essential components of the offshore energy supply chain. Their performance depends on the ability to process and liquefy hydrocarbons onboard and transfer them safely to carrier vessels in open seas [1]. Side-by-side (SBS) offloading is a widely adopted configuration, yet under certain wave conditions, piston-mode resonance may develop in the narrow gap between adjacent vessels. This resonance amplifies the free-surface elevation and induces strong hydrodynamic coupling, leading to large relative motions and potential damage to flexible transfer hoses hanging between the vessels. Similar resonance phenomena occur in other confined marine environments, such as vessel berthing and flow within ice channels [2]. Gap resonance thus remains a topic of continuing scientific and engineering interest, as its nonlinear hydrodynamic behavior governed by, e.g., viscous flow separation, remains challenging to predict efficiently, while existing experimental and numerical approaches are often economically or computationally expensive.

In the literature, research on fluid resonance in confined regions with a free surface began with theoretical analyses based on linear potential-flow theory [3–8]. These studies established fundamental understanding of modal characteristics and natural frequencies of flow motions in confined fluid domains. Laboratory experiments were later carried out to validate theoretical predictions and examine the dependence of resonant responses on geometric and wave parameters [9–18]. While potential-flow theory can predict natural frequencies of the flow motion of the water column in the gap with good accuracy, it tends to overestimate wave elevations due to the neglect of viscous damping in the model [9]. Modified potential-flow models with empirical damping terms were seen to improve the numerical predictions [11,19–27], but their accuracy relies on model calibration using experimental or high-fidelity Computational Fluid Dynamics (CFD) data [28]. With advances in computation, viscous-flow solvers based on the Navier–Stokes (NS) equations have been employed to study gap resonance under various configurations [29–39], providing deeper insights into viscous dissipation and flow separation effects.

Despite these advances, most existing studies address the influence of individual parameters—such as wave height, draft of the structure, or gap width—on gap resonance [16, 18, 40, 41], whereas the combined effects of multiple governing factors remain insufficiently explored. In practice, resonance behavior is jointly influenced by incident wave characteristics, structural geometry, and gap configuration. Performing exhaustive physical tests or CFD simulations for all parameter combinations is both time-consuming and costly. Therefore, developing a simplified predictive tool that captures the coupled effects of the dominant parameters is of great practical importance, particularly for preliminary design and feasibility assessments.

Dimensional analysis provides a powerful framework for identifying the key non-dimensional parameters governing the physics of complex problems such as gap resonances. Once these parameters are established, existing experimental and numerical data can be interpreted in a unified framework, enabling the development of simplified empirical correlations that capture the essential physical trends with minimal computational effort. When properly calibrated and validated, such formulations can efficiently facilitate engineering applications requiring quick yet reliable estimates of resonant responses.

In this study, dimensional analysis based on a simplified physical model is conducted to determine the principal non-dimensional parameters governing piston-mode resonance between two fixed identical side-by-side barges subjected to incident Stokes waves, from which it is demonstrated that wave steepness and draft-to-beam ratio are the two dominant parameters under deep-water, wave-only conditions. These have not been explicitly demonstrated in earlier studies, which typically only examine the isolated influence of individual factors, e.g., draft, wave height, or gap width, on the gap resonances, making it difficult to directly extrapolate the results to other cases with different dimensions. This study presents the first comprehensive investigation of the combined influence of wave steepness and draft-to-beam ratio on both the natural frequency and resonant response of the water column within the gap. Inspired by the analytical solution of the massless-damping-lid (MDL) model [14, 42–46] with both linear and quadratic damping terms, which yields a simplified predictive tool capable of representing the key physics documented in the literature, a physics-based empirical equation is suggested and fitted to elucidate the combined effects of both parameters, i.e. wave steepness and draft-to-beam ratio, and to provide efficient predictions of resonant responses. The proposed formulation is further extended to partially account for the influence of water depth and validated against existing experimental [16, 18] and numerical data [36], demonstrating its capability as a practical tool for rapid engineering evaluation of gap resonance. A two-dimensional (2D) fully nonlinear numerical wave tank (NWT) based on the commercial CFD software *STAR-CCM+*, which has been verified and validated in our previous studies [47, 48], will be used to provide the dataset in fitting the empirical equation, spanning thirteen draft-to-beam ratios and five wave steepness values.

The remainder of this paper is organized as follows: Section 2 presents dimensional analysis to identify the key non-dimensional parameters involved in the gap resonance. Besides, the numerical flow model applied in this work is briefly introduced. Then, the computational setup of the 2D fully nonlinear NWT is described in Section 3, followed by the introduction of the designed incident waves in Section 4. Verification and validation work against the NWT and the applied numerical models are provided in Section 5. Next, numerical results of natural frequencies of the flow motion of the water column within the gap and its resonant responses, accompanied by the discussion regarding the influences of wave steepness and draft-to-beam ratio of the barges on the gap resonance, are presented in Section 6. An empirical formula, explicitly defining the relationship between the resonant response with the above two parameters, is suggested, followed by an extension to include the effect of water depth along with further validation against experimental and numerical results. Finally, concluding remarks are summarized in Section 7.

## 2 Methodology

Following the Buckingham $\pi$-theorem [49], which emphasizes the importance of examining non-dimensional quantities in physical processes, as well as physical scaling laws, dimensional analysis is carried out in Section 2.1 to identify the non-dimensional parameters governing the resonant fluid response between two barges in the SBS configuration.

For numerical models (Sections 2.2 and 2.3), a comprehensive 2D fully nonlinear NWT is established based on the NS equations within the commercial CFD software package *STAR-CCM+*. A standard setup routine commonly utilized in both open-source [50, 51] and commercial free-surface CFD packages [52–54] is used, as illustrated in Fig. 1. To account for viscous dissipation, the Unsteady Reynolds-Averaged Navier–Stokes (URANS) turbulence model is employed within the entire NWT. The interface between the air and water phases, considered as the free surface in this study, is captured using the Volume of Fluid (VOF) multiphase model [55]. Two forcing zones are set up near the two ends of the tank, within which the numerical solutions are combined with a reference regular-wave solution provided by the applied wave theory. A blending function is employed to ensure the generation of target waves with high accuracy. Waves generated in the left forcing zone propagate through the inner domain, interact with the structure, and march into the right forcing zone at the opposite end of the tank. Within the inner domain, where the structure is located and wave-structure interaction is simulated, the numerical solutions of the NS equations remain unblended.

This is a Just Accepted version, keep updated with https://doi.org/10.26599/OCEAN.2026.9470018
*OCEAN* **2026, 2, 9470018**

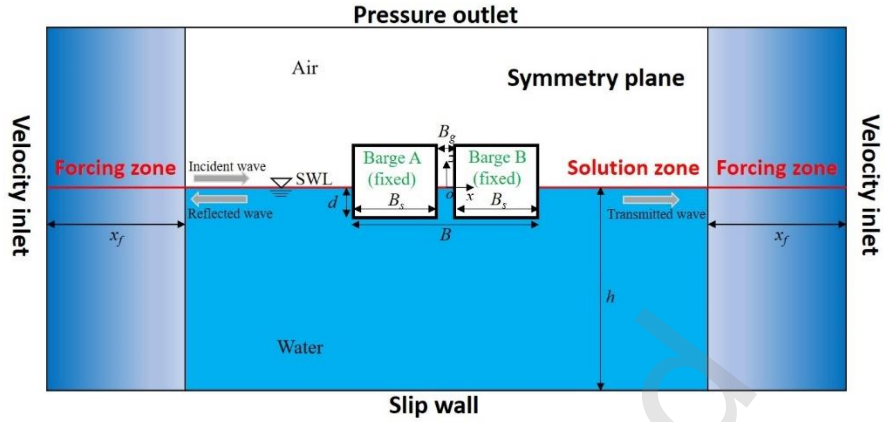


**Figure 1** A sketch of the 2D fully nonlinear NWT with two identical, fixed and SBS barges in the middle. $B_s$ is the breadth of a single barge. $B_g$ is the gap width. $B = 2B_s + B_g$ denotes the characteristic beam length of the barge system. $d$ is the identical draft of the barges. $h$ is the water depth. $x_f$ is the length of the forcing zones. 'SWL' represents the still-water level.

### 2.1 Dimensional analysis

As a premise, the fluid density ($\rho$) and gravitational acceleration ($g$) are considered as constants. Six dimensionless parameters are prone to be relevant to this gap resonance problem: $kA$, $kh$, $kB$, $d/B$, $B_g/B$ and Re. Here, $k$ and $A$ are the wavenumber and wave amplitude of the incident waves, respectively. $h$ denotes the water depth. $B = 2B_s + B_g$ represents the beam of the two barges, where $B_s$ is the breadth of a single barge and $B_g$ is the gap width. $d$ is the identical draft of the barges. Re represents the Reynolds number. In this study, we start with a deep-water condition with sufficiently large $kh$, while in Sections 6.3.2 and 6.3.3, a simple correction will be introduced to partially account for the water-depth effect, with validation against the existing experimental and numerical results. The Reynolds number has relatively less effect as the flow separation will occur at the sharp edges regardless of the Re value for the applied barge configuration when Froude-scaling the present model-scale study to full-scale realistic SBS offloading operations, as will be illustrated in the following Section 5 and Appendix E. Consequently, only four parameters are left ($kA$, $kB$, $d/B$, $B_g/B$) of concern in the following dimensional analysis.

Only the resonant piston-mode response is considered and the non-resonant conditions are of less interests in practice, Eq. (1) from Molin [4] is introduced here as a reference to determine the natural frequency of the flow motion of the water column within the gap:

$$\omega_n \approx \sqrt{\frac{g}{d+\frac{B_g}{\pi}\left[\frac{3}{2}+\ln\left(\frac{CB}{2B_g}\right)\right]}}, \tag{1}$$

where $g$ is the gravitational acceleration and $C$ is a constant slightly larger than 1.0 [4]. To simplify, $C$ is set equal to 1.0 in this study. Free-decay tests in the fully nonlinear NWT are also used to estimate the natural frequency for piston mode response, which will be introduced in the following context.

Then both sides of Eq. (1) are normalized by multiplying $\sqrt{\frac{B}{g}}$:

$$\omega_n \cdot \sqrt{\frac{B}{g}} = \sqrt{\frac{g}{d+\frac{B_g}{\pi}\left[\frac{3}{2}+\ln\left(\frac{B}{2B_g}\right)\right]}} \cdot \sqrt{\frac{B}{g}}, \tag{2}$$

and a non-dimensional natural frequency is obtained:

$$\bar{\omega}_n = \sqrt{\frac{1}{\frac{d}{B}+\frac{B_g}{B}\cdot\frac{1}{\pi}\left[\frac{3}{2}+\ln\left(\frac{B}{2B_g}\right)\right]}}. \tag{3}$$

According to the linear dispersion relation, the natural frequency can be written as:

$$\omega_n^2 = gk_n\tanh(k_nh), \tag{4}$$

where $k_n$ is the wavenumber corresponding to the natural frequency. Since the considered $k_n h$ in this study is sufficiently large and thus $\tanh(k_n h) \approx 1$, Eq. (4) can be transformed by substituting $\omega_n$ with its dimensionless counterpart $\overline{\omega}_n$:

$$\left(\overline{\omega}_n \cdot \sqrt{\frac{g}{B}}\right)^2 = g k_n. \tag{5}$$

Both sides of Eq. (5) are then square-rooted:

$$\overline{\omega}_n \cdot \sqrt{\frac{g}{B}} = \sqrt{g k_n}. \tag{6}$$

Finally, Eq. (6) is combined with Eq. (3):

$$\sqrt{\frac{1}{\frac{d}{B}+\frac{B_g}{B}\cdot\frac{1}{\pi}\left[\frac{3}{2}+\ln\left(\frac{B}{2B_g}\right)\right]}} = \sqrt{k_n B}. \tag{7}$$

As seen in Eq. (7), when resonance occurs, $k_n B$ can be determined by the other two parameters $d/B$ and $B_g/B$. Furthermore, we will only consider very narrow gaps in this study, and thus $B_g/B$ affects marginally the natural frequency of the flow motion of the water column in the gap, as will also be discussed in Section 6.1.1, and subsequently the resonant gap response. Therefore, the left-hand side of Eq. (7) becomes $\sqrt{B/d}$ as $B_g/B$ is sufficiently small, and thus the draft-to-beam ratio $d/B$ is the only primary parameter that determines $k_n B$. In summary, wave steepness $kA$ and $d/B$ are the two most important parameters governing the hydrodynamic interaction in the present study. Their influences on the natural frequency of the flow motion of the water column confined in the gap and its response at resonance will be extensively investigated in Section 6.

## 2.2 Numerical flow models

### 2.2.1 Governing equations

The governing NS equations are expressed as [56]:

$$\frac{\partial\rho}{\partial t} + \nabla\cdot(\rho\overline{\boldsymbol{v}}) = 0, \tag{8}$$

$$\frac{\partial(\rho\overline{\boldsymbol{v}})}{\partial t} + \nabla\cdot(\rho\overline{\boldsymbol{v}}\otimes\overline{\boldsymbol{v}}) = -\nabla\cdot\bar{p}\boldsymbol{I} + \nabla\cdot(\overline{\boldsymbol{T}} + \boldsymbol{T}_{st}) + \rho\boldsymbol{g} + \boldsymbol{q}_{\phi}. \tag{9}$$

Here, $\rho$ is the fluid density. $\overline{\boldsymbol{v}} = (\bar{u}, \bar{w})$ is the mean velocity vector of the fluid points. $t$ represents the time. $\otimes$ denotes the outer product. $\bar{p}$ is the mean pressure and $\boldsymbol{I}$ is the identity tensor. $\boldsymbol{g}$ is the gravity vector. $\boldsymbol{q}_{\phi}$ denotes the source term in the momentum equations and is non-zero within the forcing zone. $\overline{\boldsymbol{T}}$ represents the mean viscous stress tensor and $\boldsymbol{T}_{st}$ denotes the Reynolds stress tensor [57].

The eddy viscosity model is applied to solve $\boldsymbol{T}_{st}$ and hence provides closure of the governing equations Eqs. (8) and (9). The turbulent eddy viscosity $\mu_t$ is used to model the stress tensor as a function of mean flow quantities, known as the Boussinesq approximation [58]:

$$\boldsymbol{T}_{st} = 2\mu_t\boldsymbol{S} - \frac{2}{3}(\mu_t\nabla\cdot\overline{\boldsymbol{v}})\boldsymbol{I}. \tag{10}$$

In this study, $\mu_t$ is solved using the standard low-Re $k$-$\varepsilon$ turbulence model to decrease the turbulent viscosity near the free surface [59] with all-$y+$ wall treatment, which provides more choices of damping functions to be applied in the viscous-affected regions near walls [60]. Two additional transport equations for the kinetic energy $k_t$ and the turbulent dissipation rate $\varepsilon$ are introduced [61]:

$$\frac{\partial(\rho k_t)}{\partial t} + \nabla\cdot(\rho k_t\overline{\boldsymbol{v}}) = \nabla\cdot\left[\left(\mu + \frac{\mu_t}{\sigma_k}\right)\nabla k_t\right] + P_k - \rho(\varepsilon - \varepsilon_0), \tag{11}$$

$$\frac{\partial(\rho\varepsilon)}{\partial t} + \nabla\cdot(\rho\varepsilon\overline{\boldsymbol{v}}) = \nabla\cdot\left[\left(\mu + \frac{\mu_t}{\sigma_\varepsilon}\right)\nabla\varepsilon\right] + \frac{1}{T_e}C_{\varepsilon1}P_\varepsilon - C_{\varepsilon2}f_2\rho\left(\frac{\varepsilon}{T_e} - \frac{\varepsilon_0}{T_0}\right), \tag{12}$$

where $\sigma_k$, $\sigma_\varepsilon$, $C_{\varepsilon1}$, $C_{\varepsilon2}$ are model coefficients. $P_k$ and $P_\varepsilon$ are production terms. $T_e$ ($= k/\varepsilon$) is the large-eddy time scale. $f_2$ is a damping function. $\varepsilon_0$ is the ambient turbulence value in the source terms that counteracts turbulence decay [62], which then introduces a specific time-scale $T_0$. The default values in *STAR-CCM+* are

This is a Just Accepted version, keep updated with https://doi.org/10.26599/OCEAN.2026.9470018
*OCEAN* **2026, 2, 9470018**

applied for all these parameters related to the turbulence model [56].

To capture and update the free surface, the VOF method is employed, where the volume fraction $\alpha$ in grid cells is defined as:

$$\alpha = \begin{cases} 0, & \text{in air} \\ 0<\alpha<1, & \text{at the surface} \\ 1. & \text{in water} \end{cases} \tag{13}$$

Then the spatial variation of any fluid property $f$, e.g., the density $\rho$ and the dynamic viscosity $\mu$, can be represented as a weighted average of the quantities in both phases:

$$f = \alpha f_{\text{water}} + (1-\alpha) f_{\text{air}}, \tag{14}$$

in which the subscripts "water" and "air" denote the properties of the corresponding phases, respectively.

A transport equation for the volume fraction of water $\alpha$ is to be solved when only water and air phases are considered, which reads:

$$\frac{\partial \alpha}{\partial t} + \nabla \cdot (\alpha \overline{\boldsymbol{v}}) = 0, \tag{15}$$

and volume fraction of the air phase is adjusted to ensure that the sum of the volume fractions of the two phases is 1. For all the simulations in the present study, $\alpha = 0.5$ is adopted to mark the free surface.

### 2.2.2 Wave forcing

A wave forcing technique in *STAR-CCM+* is applied to generate waves and absorb wave reflections by smoothly enforcing the prescribed nonlinear solution over a set distance through modulating $\boldsymbol{q}_\phi$ in the source term [54]. The wave forcing applies only to the momentum equations in Eq. (9) and $\boldsymbol{q}_\phi$ can be represented as:

$$\boldsymbol{q}_\phi = -\gamma \rho (\boldsymbol{\phi} - \boldsymbol{\phi}^*). \tag{16}$$

Here, $\gamma$ denotes the forcing coefficient. Its optimum value $\gamma_{\mathrm{opt}}$ to achieve the best wave absorption can be determined according to the procedure suggested by Perić and Abdel-Maksoud [63]. $\boldsymbol{\phi}$ represents the current numerical solution of the momentum equations and $\boldsymbol{\phi}^*$ is the prescribed incident-wave solution. The velocity and volume fractions of the incident waves are defined based on the applied wave theories within the forcing zones. The length of the wave forcing zone $x_f$ can typically be chosen as $\lambda \leq x_f \leq 2\lambda$ [64]. Here $\lambda$ is the incident wavelength. The forcing coefficient varies smoothly within the forcing zone as follows:

$$\gamma(x^*) = -\gamma_{\max} \cos\left(\frac{\pi x^*}{2}\right), \tag{17}$$

in which $\gamma_{\max}$ is the maximum value of the forcing coefficient. $x^*$ is the normalized distance from the cell considered to the boundary in the direction of wave propagation with respect to the length scale of the forcing zone.

### 2.3 Numerical implementations

The above governing equations, Eqs. (8), (9), (11), (12) and (15), are solved in *STAR-CCM+* using the finite volume method, with all integrals approximated by the midpoint rule. The resulting coupled system of equations is then linearized and solved by an iterative implicit unsteady segregated solver, using a multigrid method. The second-order upwind scheme is applied for the convection terms, and the temporal discretization scheme is also of second-order accuracy. Eight inner iterations are performed in each time step to solve the governing equations for all the simulations in this study. A Courant number $C_L(= c\Delta t/\Delta x) < 0.2$ is guaranteed near the free surface to satisfy the Courant-Friedrichs-Lewy (CFL) condition. Here, $c$ denotes the celerity of incident waves. $\Delta x$ and $\Delta t$ represent the spatial and temporal resolution, respectively. For more details on

This is a Just Accepted version, keep updated with https://doi.org/10.26599/OCEAN.2026.9470018
*OCEAN* **2026, 2, 9470018**

the schemes and solvers regarding the numerical model, interested readers are referred to the book [65] or the *STAR-CCM+* user guide [56].

## 3 Computational Setup of the Numerical Wave Tank

A 2D fully nonlinear NWT, as shown in Fig. 1, is established in *STAR-CCM+* to study the effects of wave steepness $kA$ and draft-to-beam ratio $d/B$ on the gap resonance. The length of the tank is determined based on the considered incident wavelength $\lambda$. The velocities and volume fractions of wave incidence are prescribed based on the fifth-order Stokes wave solution [66] in the wave-forcing zones at both ends of the flume, each length of which is set to one incident wavelength. A pressure outlet is applied to the top boundary, with specified values as the atmospheric pressure. Only one layer of meshes is employed along the transverse direction of the 2D NWT, with the symmetry boundary conditions applied on both side walls of the flume. A slip wall condition is imposed on the sea bottom, while a no-slip wall condition is applied to both barge surfaces. The Cartesian coordinate system is located at the middle of the flume and aligned with the SWL, with waves propagating along the $x$-axis and elevating along the $z$-axis. Two identical, fixed and SBS barges are positioned at the center of the wave flume and symmetrical to the origin. Numerical simulations start from the state where theoretical solutions of the incident fifth-order Stokes waves are predefined and evolve with time.

A trimmed mesh is utilized throughout the entire domain, with a typical configuration illustrated in Fig. 2. To accurately capture the wave elevation, 20 mesh cells per wave height are employed along the vertical $z$-direction near the free surface with a size of $\Delta z$. The mesh size along the wave propagation ($x$-direction) within the free surface refinement, denoted as $\Delta x$, is chosen to maintain an aspect ratio of $\Delta x/\Delta z = 4$. Finer meshes are also adopted to record the near-barge flow field and the flow separation at the sharp corners of the barges. Meshes are further refined within the narrow gap to better resolve the wave elevation. The prism layers are extruded from the barge surfaces to resolve the boundary layer, with the near-wall $y$+ value strictly below 1.

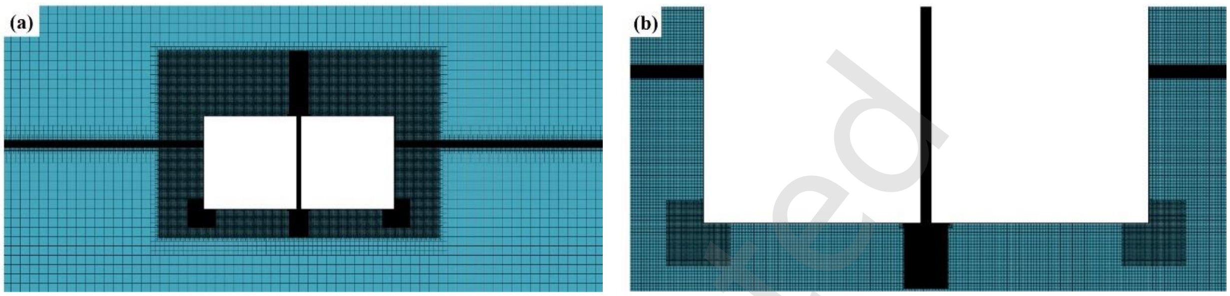


**Figure 2** Mesh configuration: (a) around the barges; (b) close to the gap.

For the free-decay model to determine the natural frequency of the flow motion of the water column in the gap, wave incidence and forcing zones are absent. The same trimmed meshes are utilized. All the dimensions of the barges and the gap within are consistent with those in the wave dynamic system.

## 4 Wave Conditions

In numerical simulations, fifth-order Stokes waves are employed as the incident waves in this study. Five values of wave steepness ($k_nA = 0.02, 0.025, 0.03, 0.035$ and $0.07$) and thirteen draft-to-beam ratios $d/B$ ranging from 0.15 to 1.00, leading to a total of 65 combinations, are considered to study the flow motion of the water column within the gap and the resonant gap response. The wave conditions are marked by scatters in Fig. 3 together with the existing wave theories, confirming that all the considered incident waves belong to deep-water waves. When $k_nA = 0.02$, the group of incident waves hit the threshold between linear and Stokes second-order waves. As $k_nA$ increases, the waves fall entirely into the regime where the Stokes second-order wave theory is applicable. Separate numerical free-decay tests have also been carried out to estimate the natural frequencies $\omega_n$ for different $d/B$.

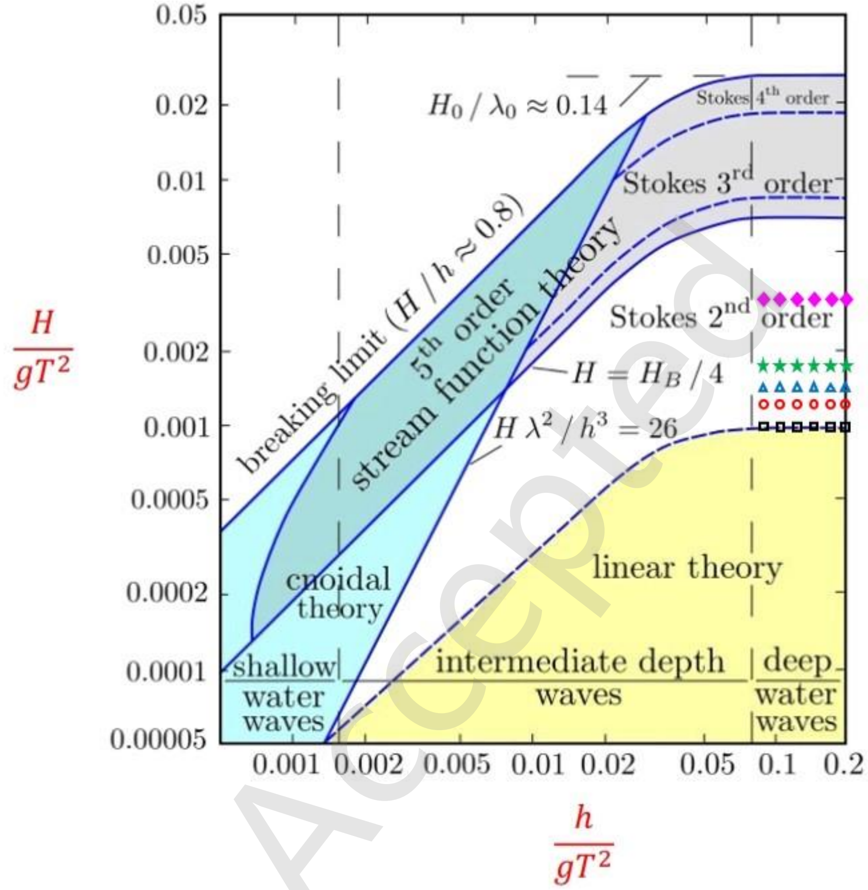


**Figure 3** Incident waves considered in the present study (reproduced under the OA CC BY 4.0 license from Le Méhauté [67] ©1976, Springer). Here, $H$ is the wave height and $T$ is the wave period. $h$ denotes the water depth. The black square, red circle, blue triangle, green star and magenta diamond represent the incident waves with $k_nA = 0.02, 0.025, 0.03, 0.035$ and $0.07$, respectively.

Considering that the dimensional analysis described in Section 2.1 is based on the linear dispersion relation, it remains questionable whether the analysis can be applied to the adopted incident waves where the second-order Stokes wave theory works. To certify, the third order dispersion relation is also considered:

$$\omega_n^2 = gk_n \cdot \underbrace{\sigma}_{\text{Part 1}} \cdot \underbrace{\left[1+\frac{9-10\sigma^2+9\sigma^4}{8\sigma^4}\left(k_n A\right)^2\right]}_{\text{Part 2}}, \tag{18}$$

where $\sigma = \tanh(k_n h)$. The high-order term, Part 2 in Eq. (18), varies between 1.0004 and 1.004 for the five considered $k_n A$ values, meaning that the linear dispersion relation is a good approximation. Therefore, the present dimensional analysis can be applied to all the designated incident waves.

## 5 Verification and Validation

The established NWT and applied numerical models have been verified and validated in our previous works [47, 48], which are summarized in Appendices A–D. For the mesh convergence study, less than 1.0 % differences are found for the time-averaged wave amplitude in the middle of the empty tank, exactly where the gap center is located with barges in the tank, for three mesh resolutions when compared to the theoretical solution of the fifth-order Stokes wave theory. For the wave-barge system, the discrepancy falls within 2.3 % for the coarse, medium, and fine mesh configurations. Therefore, the medium mesh configuration is applied for all the numerical simulations in this study. The numerical free-decay model is also validated and the coincident result, showing the largest difference of only 4.1 % with the experimental data, certifies its applicability to predict the natural frequency of the flow motion of the water column within the gap. Furthermore, the ability of the NWT to capture the piston-mode frequency of the gap when resonance occurs under wave-only conditions is justified against the validated free-decay model. In this section, only the applicability of dimensional analysis in investigating the considered gap resonance, originally proposed in this study, is validated. A series of simulations is carried out and the wave-induced responses within the gap at resonance are compared with the experimental data [16] and other numerical results

[36]. Four combinations of barge draft and gap width are selected. The barge dimension of the present numerical models is doubled relative to those used by Saitoh et al. [16] and Moradi et al. [36], corresponding to a geometric scale ratio of 2, while all the key dimensionless parameters are maintained identical. The beam-to-gap ratio is kept constant as $B/B_g = 21$, in consistent with the model tests. Only the wave elevation within the gap at resonance is considered, and the response amplitude is compared in Fig. 4.

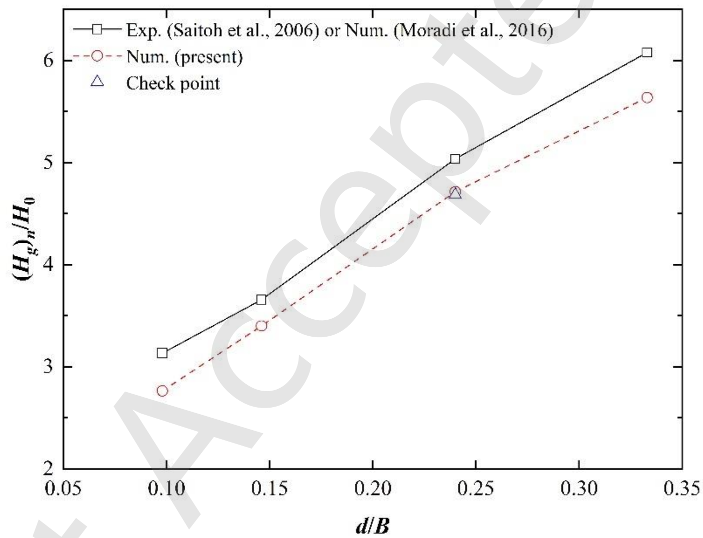


**Figure 4** Normalized wave height in the gap at resonance $(H_g)_n/H_0$ with various draft-to-width ratios of the barges $d/B$. $(H_g)_n$ is the crest-to-trough wave height in the gap at its resonance. $H_0$ is the incident wave height. The blue triangle is a checkpoint, representing the result of the present numerical model using the same size of barge models as the experiments [16] and numerical simulations [36]. All the other results are based on model setup with twice the size of those in Saitoh et al. [16] and Moradi et al. [36].

As shown in the figure, the present numerical results agree with both the experimental measurements and previous numerical solutions. The corresponding relative discrepancies are summarized in Table 1. The largest difference of $+11.5\%$ is observed at $d/B = 0.10$. To further examine possible scale effects, an extra simulation is conducted using the same size of barge models as the experiments in Saitoh et al. [16] at $d/B = 0.24$, represented by the 'Check point' in Fig. 4. The results show that the observed discrepancies do not originate from the scale effects, but possibly from the numerical uncertainties in the applied CFD model and experimental errors in the model tests. As discussed, the satisfactory comparison confirms that the dimensional analysis introduced in Section 2.1 provides a reasonable basis to investigate the gap resonance problem under wave-only conditions.

**Table 1** Relative difference $E(\%)$ of non-dimensional resonant gap responses between the present model and experimental or other numerical solutions. $k_n$ is the resonant wavenumber and $A_0$ denotes the incident wave amplitude. $h$ represents the water depth. The result in parentheses at $d/B = 0.24$ corresponds to that of the 'Check point' in Fig. 4.

| $d/B$ | $k_nA_0$ | $d/h$ | $(H_g)_n/H_0$ (Present) | $(H_g)_n/H_0$ (Exp. or Num.) | $E(\%)$ |
|---|---|---|---|---|---|
| 0.10 | 0.066 | 0.21 | 2.77 | 3.13 | $-11.50$ |
| 0.15 | 0.052 | 0.31 | 3.40 | 3.66 | $-7.10$ |
| 0.24 | 0.037 | 0.50 | 4.71 (4.69) | 5.04 | $-6.55$ ($-6.94$) |
| 0.33 | 0.030 | 0.70 | 5.64 | 6.08 | $-7.24$ |

Moreover, a sensitivity study is carried out to demonstrate the Re effect on the resonant gap response, the details of which are demonstrated in Appendix E. This is achieved by changing the kinematic viscosities of water and air in the numerical simulations, while all other settings remain unchanged. As discussed, for the critical case considered in the present study ($k_nA = 0.02$ and $\frac{d}{B} = 0.98$), the Re value indeed affects the resonant gap responses when Re $\approx 1.0 \times 10^6$, after which the response is less sensitive with Re within the considered Re range (from $6.7 \times 10^4$ to $1.0 \times 10^7$). However, the numerical result presented in this study is derived at a model scale. When Froude scaling to a full-scale ship, the Re value will fall into the regime where the resonant gap response is insensitive to Re. Therefore, the Reynolds number has less effect on the response amplitude of free-surface elevation within the narrow gap at resonance during the realistic scenario of marine operations.

# 6 Results and Discussions

According to the dimensional analysis described in Section 2.1, two key parameters, wave steepness $kA$ and draft-to-beam ratio $d/B$, are identified as the primary factors influencing the gap response at resonance. To investigate the combined effects of these two parameters, it is first crucial to accurately determine the natural frequency ($\omega_n$). Accordingly, free-decay tests are conducted in Section 6.1 to examine the isolated effects of gap-to-beam ratio $B_g/B$ and draft-to-beam ratio $d/B$ on $\omega_n$. Based on the results, a relatively small $B_g/B$ is chosen, lower than which $\omega_n$ remains sufficiently close to its asymptotic value with $B_g/B \to 0$.

Inspired by the MDL model, the isolated and combined effects of $d/B$ and $k_nA$ on the resonant gap response are investigated in Section 6.2 and Section 6.3.1, respectively, with an empirical fitting equation derived to estimate the resonant gap responses. The obtained equation is further corrected in Section 6.3.2, following the linear potential-flow theory, to partially account for the influence of water depth $k_nh$. Finally, the proposed formulation is validated in Section 6.3.3 by comparison with the experimental data and the results of both the present and previous numerical models.

## 6.1 Gap natural frequency

### 6.1.1 Effect of beam-to-gap ratio $B/B_g$

Ten gap widths $B_g$ are selected with the identical beam size of each barge $B_s$, thus

$B = 2B_s + B_g$ varies with $B_g$, leading to the variation of $B_g/B$ from 0.005 to 0.048. The draft of both barges is kept constant as $0.5B_s$. The normalized natural frequencies are obtained using the present free-decay model, as shown in Fig. 5. The solutions by the analytical formula Eq. (1) are also included. It is observed that the results of the present free-decay model are close to the analytical solutions, with the largest relative difference of only $-1.9\%$ at the maximum $B_g/B = 0.048$.

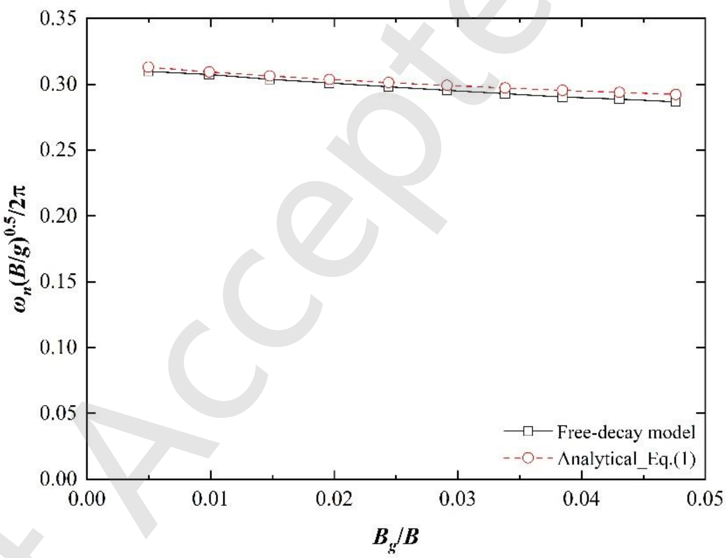


**Figure 5** Non-dimensional natural frequencies of the flow motion of the water column within the gap with various gap-to-beam ratios $B_g/B$.

In generally, the natural frequency decreases with the gap-to-beam ratio. When the gap width is relatively small, the strong boundary effect tends to confine the wave motion within the gap. The path of wave propagation within the gap is also short. These result in a higher natural frequency. The natural frequency becomes more sensitive to the increase of gap width. The boundary effects weaken and the formation of standing waves within a wider gap becomes harder, leading to a reduction in the natural frequency.

Since the effect of the gap-to-beam ratio on the resonant gap response is not considered in the present study, an appropriate $B_g/B$ should be adopted that yields an insignificant impact on the natural frequency and thus the resonant gap response. As shown in the figure, the variation of the gap width will not excessively affect the natural frequency when $B_g/B < 0.024$, i.e. $B/B_g > 41$. Therefore, the beam-to-gap ratio $B/B_g$ is set as 41 in all the following simulations.

#### 6.1.2 Effect of draft-to-beam ratio $d/B$

For the draft-to-beam ratio $d/B$, nine different values, varying between 0.049 and 0.44, are considered. Here, $d$ varies solely and $B$ is kept identical. The normalized natural frequencies are attained from the numerical free-decay tests and compared with Molin's analytical formula [4] (see also Eq. (1)) in Fig. 6. Coincident results are observed, and the numerical results converge more to the analytical ones as the draft increases. At a lower $d/B$, i.e. with a small draft, the natural frequency exhibits a rapid decrease. A small draft means less mass of water confined in the gap, leading to faster oscillation of gap fluid and, consequently, higher sensitivity of the natural frequency to the draft. As $d/B$ increases, the rate of decrease slows down and begins to level off. On the other hand, the natural frequencies obtained by the present free-decay model are applied in the next Section 6.2 to investigate the effects of draft-to-beam ratio $d/B$ and wave steepness $kA$ on the resonant gap response.

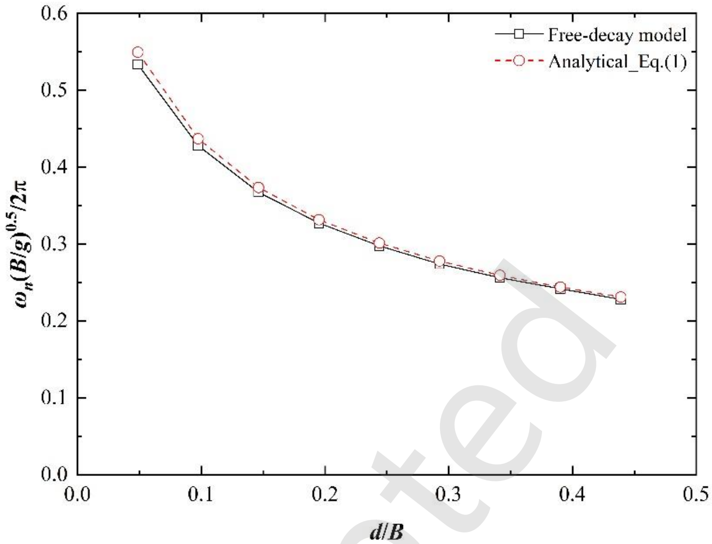


**Figure 6** Non-dimensional natural frequencies of the flow motion of the water column in the gap with various draft-to-beam ratios $d/B$.

## 6.2 Gap response at resonance

Numerical simulations are carried out to investigate the isolated effects of the draft-to-beam ratio and wave steepness on the amplitude of free surface elevation in the gap at resonance under wave conditions. The beam-to-gap ratio $B/B_g$ is set constant as 41 and the water depth is regarded as sufficiently large. Based on the natural frequencies in Fig. 6, the corresponding wavenumbers at resonance can be obtained according to Eq. (6).

### 6.2.1 Effect of draft-to-beam ratio $d/B$

Figure 7 shows the normalized wave heights in the gap at resonance under five values of wave steepness ($k_nA = 0.02, 0.025, 0.03, 0.035$ and $0.07$) for a range of draft-to-beam ratios. At the start, the resonant gap response gradually rises with $d/B$. As $d/B$ goes beyond 0.6, the response tends to stabilize at a certain value, indicating that the gap resonance is less sensitive to $d/B$ if it is sufficiently large. This can be attributed to the lower excitation force acting on the gap fluid. When the barge draft is larger, the wave dynamics become weaker at the level of the gap entrance, exciting a smaller dynamic pressure there. Overall, five groups of results with different wave steepness exhibit a similar trend, while the responses for a smaller $k_nA$ are higher than those for larger $k_nA$. This is due to the presence of quadratic damping, as will be explained later in Section 6.2.2.

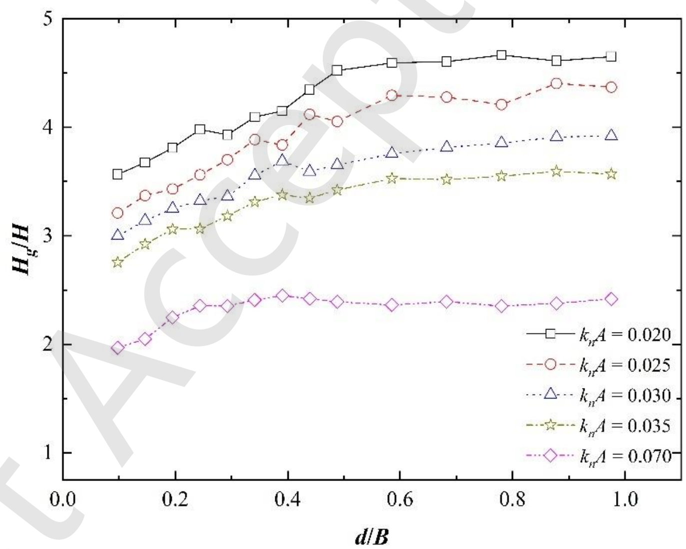


**Figure 7** Non-dimensional resonant gap responses $H_g/H$ with various draft-to-beam ratios $d/B$ under waves with different steepness $k_nA$. $H$ is the incident wave height and $A = H/2$ is the wave amplitude.

### 6.2.2 Effect of wave steepness $kA$

The results of resonant gap responses in Fig. 7 are reorganized and shown in an alternative form to illustrate their dependence on the wave steepness. As shown in Fig. 8, the non-dimensional wave heights $H_g/H$ within the gap at resonance exhibit a nonlinear decrease with increasing $k_n A$ for different $d/B$. This behavior can be explained by the MDL model, applied in Fournier et al. [43]. The steady-state motion response in this model is described by a linear-harmonic-operator (LHO) system (see Eq. (194) in Newman [68]):

$$A_{33}\ddot{\eta}_3(t) + B_{33}\dot{\eta}_3(t) + C_{33}\eta_3(t) = F_{\mathrm{ex}}(t), \tag{19}$$

where $A_{33}$ denotes the heave-heave added mass of the lid confined by the two barges. $B_{33}$ and $C_{33}$ are the corresponding damping and restoring coefficients of the gap-flow system. In case the damping force is nonlinear, $B_{33}$ is understood as the linearized equivalent damping coefficient, including all damping sources. $F_{\mathrm{ex}}(t)$ and $\eta_3(t)$ represent the wave excitation force and heave motion of the lid, respectively.

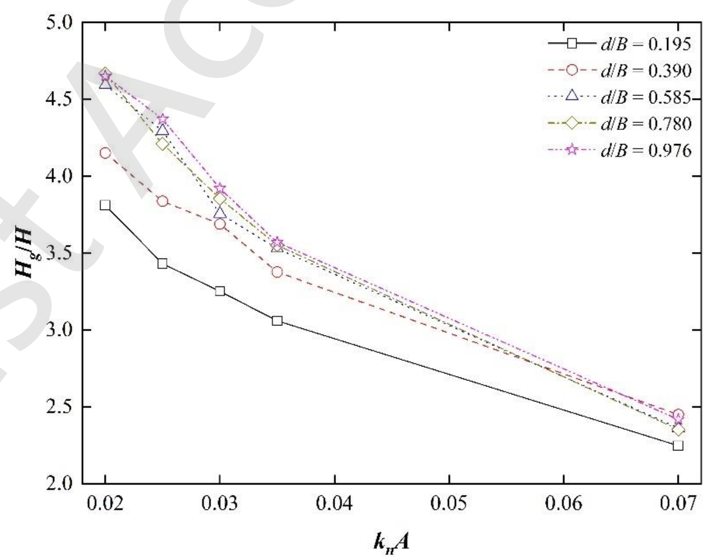


**Figure 8** Normalized resonant gap responses with various wave steepness $k_n A$ for different draft-to-beam ratios $d/B$.

A steady-state solution is pursued here, meaning that all transient effects have died out due to the presence of damping. The system is subjected to a time-harmonic excitation force in heave, expressed as $F_{\mathrm{ex}}(t) = \mathrm{Re}\{AX_3\mathrm{e}^{\mathrm{i}\omega t}\}$, where $\omega$ is the oscillating frequency. Here, $\mathrm{Re}\{\cdot\}$ denotes the real part of a complex number. $A$ is the incident wave amplitude and $X_3$ is the complex excitation force coefficient per unit wave amplitude. The imaginary unit is denoted by i. The steady-state solution to Eq. (19) is time-harmonic at the same frequency as $F_{\mathrm{ex}}(t)$, given by $\eta_3(t) = \mathrm{Re}\{\xi_3\mathrm{e}^{\mathrm{i}\omega t}\}$, where $\xi_3$ represents the complex heave amplitude of the lid. By inserting the excitation force and heave response into Eq. (19), $\xi_3$ can be obtained as follows:

$$\xi_3 = \frac{AX_3}{-A_{33}\omega^2+\mathrm{i}B_{33}\omega+C_{33}}. \tag{20}$$

Since $C_{33} = \omega_n^2 \cdot A_{33}$ at resonance, the non-dimensional heave amplitude of the free surface in the gap at the natural frequency can be obtained:

$$\frac{|\xi_3|}{A} = \frac{|X_3|}{\omega_n B_{33}}. \tag{21}$$

Here, $B_{33}$ consists of two contributions: a linear damping ($B_l$) mainly due to wave radiation and friction within the boundary layer between the gap flow and the barges, which can be related to the excitation force coefficient $|X_3|$, and an equivalent damping ($B_q$) due to quadratic force caused by viscous flow separation. If the quadratic damping force is $F_d = -b_q\dot{\eta}_3|\dot{\eta}_3|$, $B_q$ can be estimated as $B_q = \frac{8}{3\pi}b_q\omega_n|\xi_3|$ based on energy conservation. Here, $b_q$ is the quadratic damping coefficient. Therefore, Eq. (21) is rewritten as:

$$\frac{|\xi_3|}{A} = \frac{|X_3|}{\omega_n(B_l+B_q)} = \frac{|X_3|}{\omega_n B_l+\frac{8}{3\pi}b_q\omega_n^2|\xi_3|}. \tag{22}$$

Then a quadratic equation of $|\xi_3|$ is obtained:

$$\frac{8}{3\pi} b_q \omega_n^2 |\xi_3|^2 + \omega_n B_l |\xi_3| - A|X_3| = 0, \tag{23}$$

for which the two roots can be analytically defined. Using the deep-water dispersion relation $\omega_n^2 = gk$, and taking only the positive root of Eq. (23), we have:

$$\frac{|\xi_3|}{A} = \frac{2|X_3|}{\sqrt{gk}\left(B_l + \sqrt{B_l^2 + \frac{32}{3\pi} b_q A |X_3|}\right)} = \frac{|\bar{X}_3|}{1 + \sqrt{1 + \alpha \cdot (kA)}}, \tag{24}$$

where the following non-dimensional variables have been defined:

$$|\bar{X}_3| = \frac{2|X_3|}{B_l \sqrt{gk}} \quad \text{and} \quad \alpha = \frac{32}{3\pi} \frac{b_q |X_3|}{k B_l^2}. \tag{25}$$

In this study, we consider very narrow gap with sufficiently small $B_g/B$. As a leading order approximation, the terms $|X_3|$, $B_l$ and $b_q$ are linearly proportional to the gap width $B_g$. Therefore, the $B_g$-dependent terms cancel out in the expressions of $|\bar{X}_3|$ and $\alpha$ respectively, and thus these two parameters are independent on $B_g$. This explains why $B_g/B$ is not considered as an important non-dimensional parameter in our dimensional analysis in Sect. 2.1 as long as $\frac{|\xi_3|}{A}$ is concerned.

In summary, the dependency of $\frac{|\xi_3|}{A}$ on the wave steepness is explicitly defined in Eq. (24), where according to our dimensional analysis, the other variables $|\bar{X}_3|$ and $\alpha$, are primarily dependent only on the draft-to-beam ratio $d/B$.

While Eq. (24) represents an exact solution for Eq. (23), two special cases can be checked. If linear damping dominates, which means $B_l \gg B_q$, and thus $\alpha \to 0$, Eq. (24) leads to:

$$\frac{|\xi_3|}{A} \approx \frac{|\bar{X}_3|}{2} \propto (kA)^0. \tag{26}$$

The right-hand side of Eq. (26) does not explicitly depend on $kA$.Therefore, based on the dimensional analysis in Section 2.1, $\frac{|\xi_3|}{A}$ primarily depends on $d/B$ if linear damping dominates.

On the other hand, when $B_q$ dominates the damping with $B_q \gg B_l$ and thus $\alpha \gg 1$, we get:

$$\frac{|\xi_3|}{A} \approx \frac{|\bar{X}_3|}{\sqrt{\alpha \cdot (kA)}} = \sqrt{\frac{3\pi}{8g} \frac{|X_3|}{b_q(kA)}}. \tag{27}$$

In this case, $\frac{|\xi_3|}{A}$ depends not only on $d/B$ but is inversely proportional to $\sqrt{kA}$. In Section 6.3, the combined effects of $d/B$ and $kA$ on resonant gap responses will be discussed. The form of the solution in Eq. (24) will be utilized to develop an empirical equation to fit the numerical results in Figs. 7 and 8.

## 6.3 An empirical equation for non-dimensional gap responses at resonance

### 6.3.1 Dependence on $d/B$ and $kA$

Applying a least-square fitting to the numerical results in Fig. 7 for a range of $d/B$ and $kA$, an empirical equation can be developed as a quick tool to predict the resonant gap responses for the considered SBS configuration. As discussed in Section 6.2.2, the non-dimensional coefficients $|\bar{X}_3|$ and $\alpha$ in Eq. (25) are primarily only functions of $d/B$, i.e. $|\bar{X}_3| = f_1\left(\frac{d}{B}\right)$ and $\alpha = f_2\left(\frac{d}{B}\right)$. Since wave kinematics decay with vertical distance to water surface, the wave excitation force coefficient $|X_3|$ decreases monotonically with $d/B$ if $B$ is kept constant, meaning that the corresponding non-dimensional parameter $|\tilde{X}_3|$ also decreases with $d/B$. The same applies for the linear damping $B_l$. We introduce the following non-dimensional form for $|X_3|$, $B_l$ and $b_q$:

$$|\tilde{X}_3| = \frac{|X_3|}{\rho g B_g}, \quad \tilde{B}_l = \frac{B_l}{\rho g B_g \sqrt{B/g}} \quad \text{and} \quad \tilde{b}_q = \frac{b_q}{\rho B_g}. \tag{28}$$

Based on Eq. (1), the natural frequency $\omega_n$ is inversely proportional to $\sqrt{d/B}$ when

$B_g/B$ is sufficiently small. Plugging Eqs. (28) and (6) in Eq. (25), we get:

$$|\bar{X}_3| = f_1\left(\frac{d}{B}\right) = \frac{2|X_3|}{B_l\sqrt{gk}} = \frac{2\rho g B_g|\tilde{X}_3|}{(\tilde{B}_l\rho g B_g\sqrt{B/g})\cdot(\varpi_n\sqrt{g/B})} = \frac{2}{\tilde{B}_l}\frac{|\tilde{X}_3|}{}\frac{1}{\varpi_n}, \quad (29)$$

where $|\tilde{X}_3|$, $\tilde{B}_l$ and $\varpi_n$ depend primarily on $d/B$.

Similarly, the coefficient $\alpha = f_2\left(\frac{d}{B}\right)$ can also be expressed as:

$$\alpha = f_2\left(\frac{d}{B}\right) = \frac{32}{3\pi}\frac{b_q|X_3|}{kB_l^2} = \frac{32}{3\pi}\frac{|\tilde{X}_3|\tilde{b}_q}{\tilde{B}_l^2} = \frac{32}{3\pi}\frac{|\tilde{X}_3|}{\tilde{B}_l}\frac{\tilde{b}_q}{\tilde{B}_l}\frac{1}{\varpi_n^2}. \quad (30)$$

Based on Eqs. (29) and (30), we will propose empirical expressions for $|\tilde{X}_3| = f_1\left(\frac{d}{B}\right)$ and $\alpha = f_2\left(\frac{d}{B}\right)$ that will be used to fit the numerical results of the CFD simulations in Fig. 7. When looking at the common term $\frac{|\tilde{X}_3|}{\tilde{B}_l}$ which appeared in Eqs. (29) and (30), since both $|\tilde{X}_3|$ and $\tilde{B}_l$ decrease with $d/B$, we will approximate $\frac{|\tilde{X}_3|}{\tilde{B}_l} \approx a_1\frac{d}{B} + a_2$. Here, $a_1$ and $a_2$ are constants. In fact, if the incident wavelength is much longer than the dimensions of the structures, it can be shown using the long-wave approximation (see Eq. (163) in Newman [68]) that both $|\tilde{X}_3|$ and $\tilde{B}_l$ decay exponentially with $d/B$ as $\mathrm{e}^{-kd} = \mathrm{e}^{-kB\cdot\frac{d}{B}} = \mathrm{e}^{-\varpi_n^2\frac{d}{B}}$. For $\varpi_n$, we can write it as $\varpi_n = \sqrt{\frac{1}{\frac{d}{B}+c_1}}$ according to Eq. (3) where $c_1$ is another constant. Finally, $\tilde{b}_q$ is expected to have a very week dependence on $d/B$. Therefore, we can also approximate $|\bar{X}_3|$ and $\alpha$ as:

$$|\bar{X}_3| = \left(a_1\frac{d}{B} + a_2\right)\sqrt{\frac{d}{B} + c_1}$$
$$\text{and } \alpha = b_1\left(a_1\frac{d}{B} + a_2\right)\left(\frac{d}{B} + c_1\right)e^{\left[c_1\left(\frac{d}{B}\right)^{-1}+1\right]^{-1}}. \quad (31)$$

Therefore, an plausible empirical formula inspired by Eq. (24) could be:

$$\frac{|\xi_3|}{A}=\frac{f_1\left(\frac{d}{B}\right)}{1+\sqrt{1+f_2\left(\frac{d}{B}\right)\cdot(k_nA)}}=\frac{\left(a_1\frac{d}{B}+a_2\right)\sqrt{\frac{d}{B}+c_1}}{1+\sqrt{1+b_1\left(a_1\frac{d}{B}+a_2\right)\left(\frac{d}{B}+c_1\right)e^{\left[c_1\left(\frac{d}{B}\right)^{-1}+1\right]^{-1}}\cdot(k_nA)}},\tag{32}$$

where $a_1$, $a_2$, $b_1$ and $c_1$ are the unknown coefficients to be fitted based on the numerical results in Figs. 7 and 8.

Figure 9 demonstrates the 3D least-square fitted surface of the normalized wave crests $\frac{|\xi_3|}{A}=R(d/B,k_nA)$ in the gap at resonance with a group of $d/B$ and $k_nA$ combinations considered in the present study. The numerical results in Fig. 7 obtained by the present CFD model are also included and denoted as scatters. It is observed that the fitting performs very well, with the numerical results close to the fitted surface. The normalized sum of the squares of the residuals, defined by $\bar{S}^2=\frac{\sum_{i=1}^{N}\left[\left(\frac{H_g}{H}\right)_i^{\mathrm{fit}}-\left(\frac{H_g}{H}\right)_i^{\mathrm{num}}\right]^2}{\sum_{i=1}^{N}\left[\left(\frac{H_g}{H}\right)_i^{\mathrm{num}}\right]^2}$, is as small as 0.0007. Here, $N=65$ denotes the number of data points applied for the fitting. $\left(\frac{H_g}{H}\right)_i^{\mathrm{fit}}$ and $\left(\frac{H_g}{H}\right)_i^{\mathrm{num}}$ represent the results by the fitted equation and the CFD simulations, respectively. The fitted coefficients in Eq. (32) are listed in Table 2. Furthermore, the results in Fig. 7 are again repeated here in Fig. 10 to compare with the fitted results (represented by curves), which clearly illustrate satisfactory performance of the empirical fitted equation.

**Table 2** Fitted coefficients in Eq. (32) using the least-square fitting to the present numerical results by CFD simulations.

| $a_1$ | $a_2$ | $b_1$ | $c_1$ |
|---|---|---|---|
| 11.19 | 77.85 | 62.21 | $-0.03$ |

This is a Just Accepted version, keep updated with https://doi.org/10.26599/OCEAN.2026.9470018
***OCEAN* 2026, 2, 9470018**

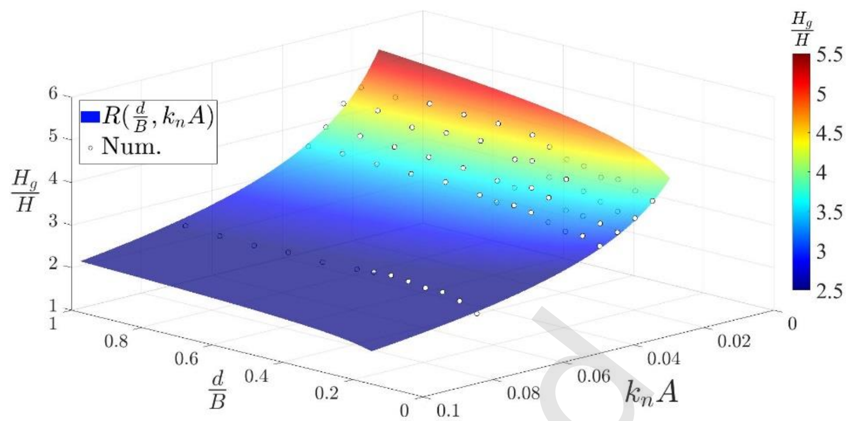


**Figure 9** 3D fitted surface of the normalized resonant gap response $\frac{|\xi_3|}{A} = R(d/B, k_n A)$ as function of the draft-to-beam ratio $d/B$ and wave steepness $k_n A$. The open circles represent the present numerical results displayed in Fig. 7.

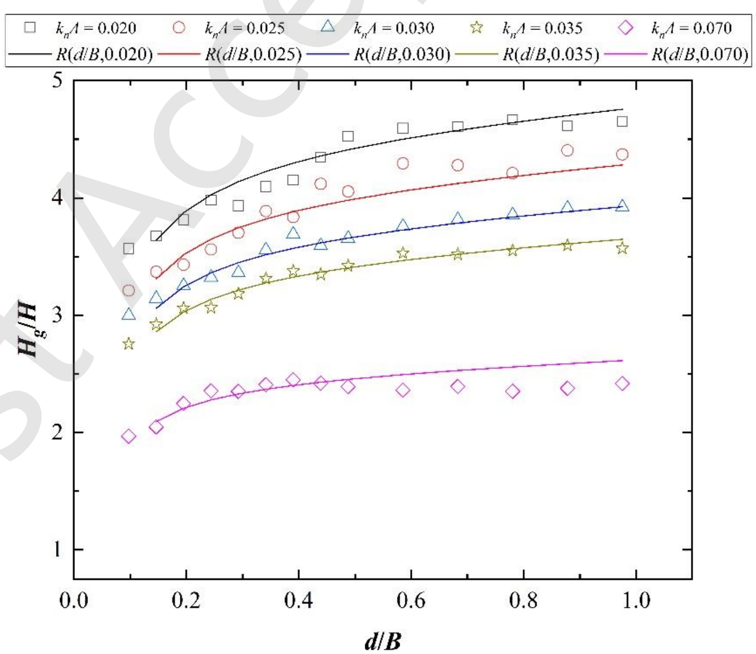


**Figure 10** Fitted curves of the normalized resonant gap response $\frac{|\xi_3|}{A} = R(d/B, k_n A)$ as function of the draft-to-beam ratio $d/B$ and wave steepness $k_n A$. The scatters represent the present numerical results displayed in Fig. 7.

With the empirical formula in Eq. (32) and the coefficients given in Table 2, we can compare the relative importance of the quadratic damping and the linear damping by considering the ratio between them:

$$\frac{B_q}{B_l} = \frac{\alpha}{|\bar{X}_3|} \cdot \frac{3\pi}{16} \cdot \sqrt{\frac{k_n}{g}} \cdot \frac{8}{3\pi} \cdot \sqrt{g k_n} \cdot |\xi_3| = \frac{1}{2}(k_n A)\frac{|\xi_3|}{A}\frac{\alpha}{|\bar{X}_3|}. \tag{33}$$

For the considered ranges of $d/B$ and $k_n A$, $\frac{B_q}{B_l}$ is found to vary between 2.72 and 15.52. In general, this ratio becomes larger for larger $d/B$ and $k_n A$, indicating that the dominant contribution of quadratic damping is expected under such scenarios. This can be explained as follows. With a larger $d/B$, the piston motion of the water column in the gap makes smaller waves, leading to smaller wave-radiation damping $B_l$ whereas $B_q$ is insensitive to $d/B$. On the contrary, $B_q \sim b_q \omega_n |\xi_3|$ will be larger for a larger $k_n A$, while $B_l$ is less dependent on $k_n A$.

### 6.3.2 Modification of fitted equation regarding water depth $kh$

Since the above-mentioned numerical results and fitted formula are derived under an infinite water depth. To roughly account for the water-depth effect on the resonant gap response but without introducing $kh$ as the third non-dimensional parameter, an extra $kh$-related term will be explicitly supplemented into the fitted formula Eq. (32), based on the linear wave theory.

For the considered dynamic SBS wave-barge system, the wave excitation force, $F_{\mathrm{ex}}(t)$ in Eq. (19), to induce the oscillation of the gap fluid mainly comes from the hydrodynamic pressure along the gap entrance [42]. For deep water, the amplitude of the hydrodynamic pressure of the incident wave at the level of the gap entrance (draft $d$) is represented as:

$$p_{dw} = \rho g A \mathrm{e}^{-kd} \cos\theta. \tag{34}$$

Here, $\rho$ is the density of water and $\theta$ is the wave phase. $p_{dw}$ will contribute to the Froude-Krylov part of $F_{\mathrm{ex}}$. However, with finite water depth, the pressure becomes:

$$p_{fw} = \rho g A \frac{\cosh[k(h-d)]}{\cosh kh} \cos\theta. \tag{35}$$

The ratio between these two pressures is defined as:

$$\beta = \frac{p_{fw}}{p_{dw}} = \frac{\cosh[k(h-d)]}{\cosh kh} \cdot \mathrm{e}^{kd} = \frac{\mathrm{e}^{2kh}+\mathrm{e}^{2kd}}{\mathrm{e}^{2kh}+1}. \tag{36}$$

Therefore, the fitted formula Eq. (32) is modified to consider the water-depth effect on the excitation force as:

$$\begin{aligned} \frac{|\xi_3|}{A} &= R\left(\frac{d}{B}, k_n A, k_n h\right) \approx R\left(\frac{d}{B}, k_n A\right) \cdot \beta \\ &= \frac{\left(a_1 \frac{d}{B} + a_2\right)\sqrt{\frac{d}{B} + c_1}}{1 + \sqrt{1 + b_1\left(a_1 \frac{d}{B} + a_2\right)\left(\frac{d}{B} + c_1\right) \mathrm{e}^{\left[c_1\left(\frac{d}{B}\right)^{-1} + 1\right]^{-1}} \cdot (k_n A)}} \cdot \frac{\mathrm{e}^{2kh}+\mathrm{e}^{2kd}}{\mathrm{e}^{2kh}+1}. \end{aligned} \tag{37}$$

Since $h > d$ and $k_n d > 0$, $\beta$ is no less than 1. When $k_n h$ is sufficiently large, $\beta \approx 1$ and thus Eq. (37) becomes the same as Eq. (32) originally developed for deep water. To show the necessity of considering the effect of water depth, extra simulations are carried out for various intermediate water depths $k_n h$, and the numerical results are compared with the modified formula Eq. (37) in Fig. 11. In these cases, $d/B$ and $k_n A$ are kept constant. Notably, $k_n$ varies with water depth, the values of which are derived from the present free-decay tests. In the figure, the wave amplitude within the gap at resonance experiences a sharp rise as the water becomes shallower due to the rapid increase in excitation forces at the level of gap entrance [35, 36, 69]. The modified equation Eq. (37) follows the same trend as the CFD results and the difference becomes smaller when the water depth increases, while the original expression Eq. (32) is independent of water depth and the fitted results deviate far from the CFD ones when water is shallower, indicating the importance of involving water depth in predicting the resonant gap responses. When comparing the fitted result by Eq. (37) to those of the CFD simulations, a larger deviation is observed for smaller water depth, with about 19.4% smaller value obtained at $k_n h = 1.89$. The reason is that the simple water-depth correction factor $\beta$ in Eq. (36) can only account for part of the water-depth effects, which is based on the vertical decay rate of the Froude-Krylov excitation force.

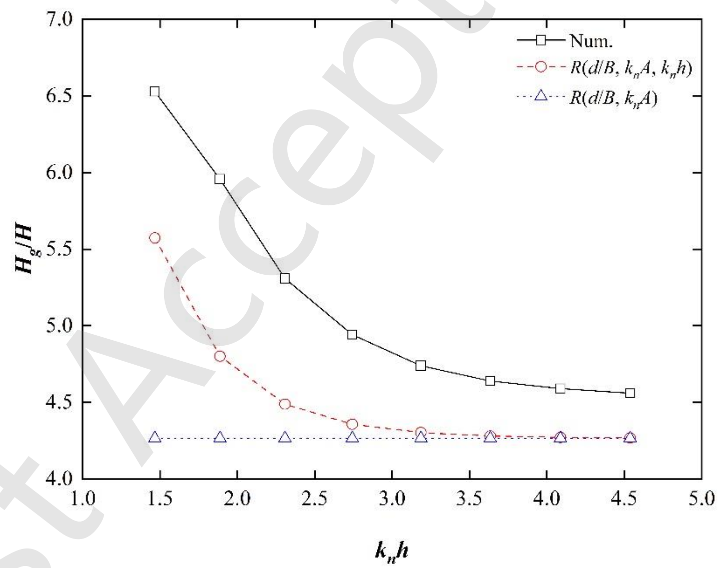


**Figure 11** Normalized resonant gap responses $H_g/H$ with $k_n h$ at the draft-to-beam ratio $d/B = 0.488$ and wave steepness $k_n A = 0.02$. The black solid line with a square denotes the numerical results obtained by the present CFD model. The red dashed line with a circle and the blue dotted line with a triangle represent the values calculated by the fitted formulas with and without the water-depth modification, i.e. Eq. (37) and Eq. (32), respectively.

### 6.3.3 Validation against other experimental and numerical results

To examine the applicability of the proposed empirical formula Eq. (37), we compare its prediction of wave amplitudes in the gap at resonance with other existing experiments [16, 18] and numerical simulations [36], as listed in Table 3. The values of $d/B$, $k_nA$ and $B/B_g$ are also provided. As demonstrated, the results derived by the fitted equation agree well with those by experiments and numerical simulations under large $k_nh$, (e.g., $k_nh \geq \pi$). For two deep-water cases ($k_nh = 7.630$ and $9.810$), the fitted results are about 12% higher than the numerical solutions of Moradi et al. [36], which is unexpected. This is attributed partly to the numerical error in Moradi et al. [36] and partly to the error of the presented empirical formula. The latter predicts consistently constant non-dimensional responses for $k_nh \geq \pi$, which agree with the trend of our high-fidelity CFD results in Fig. 11. On the contrary, the numerical results by Moradi et al. [36] show a dramatic decrease at $k_nh = 7.630$ and $9.810$, which seems to contradict with the underlying physics. When the water depth is sufficiently large, the incident and scattered waves cannot 'feel' the presence of the gap, and thus the results should tend to their deep-water asymptotes. The comparison also shows that Eq. (37) can predict the resonant gap responses at smaller $k_nA$, (e.g., $k_nA < 0.1$).

**Table 3** Comparison of resonant gap responses by the fitted formula with those by experiments and numerical simulations under $k_nh \geq \pi$.

| Case | $d/B$ | $k_nA$ | $k_nh$ | $B/B_g$ | $H_g/H$ | $R$ | $E(\%)$ |
|---|---|---|---|---|---|---|---|
| Saitoh et al. [16] (exp.) | 0.102 | 0.096 | 4.000 | 101.00 | 1.637 | 1.591 | $-2.823$ |
| Ning et al. [18] (exp.) | 0.159 | 0.136 | 3.400 | 21.00 | 2.200 | 1.515 | $-31.14$ |
| Moradi et al. [36] (num.) | 0.143 | 0.036 | 4.449 | 21.00 | 2.661 | 2.724 | $+2.366$ |
| | 0.143 | 0.036 | 5.932 | 21.00 | 2.594 | 2.723 | $+4.990$ |

| | | | | | | |
|---|---|---|---|---|---|---|
| 0.238 | 0.030 | 3.693 | 21.00 | 3.455 | 3.262 | −5.588 |
| 0.238 | 0.030 | 4.924 | 21.00 | 3.423 | 3.258 | −4.811 |
| 0.238 | 0.030 | 6.173 | 21.00 | 3.327 | 3.253 | −2.200 |
| 0.238 | 0.030 | 7.406 | 21.00 | 2.990 | 3.253 | +8.812 |
| 0.333 | 0.026 | 3.249 | 21.00 | 3.966 | 3.635 | −8.335 |
| 0.333 | 0.026 | 4.368 | 21.00 | 3.941 | 3.605 | −8.535 |
| 0.333 | 0.026 | 7.630 | 21.00 | 3.214 | 3.606 | +12.18 |
| 0.333 | 0.026 | 9.810 | 21.00 | 3.222 | 3.606 | +11.90 |

It should be noted that the fitted relation in Eq. (37) is obtained under the assumptions of deep water, small wave steepness and large beam-to-gap ratio. Accordingly, when Eq. (37) is applied to the experimental and numerical cases that do not satisfy these assumptions, reduced accuracy is expected. For example, Table 3 also presents a case with $k_n A = 0.136$ in Ning et al. [18] where Eq. (37) substantially underpredicts the response. This bias is likely due to the fact that the fitting used only numerical results with $k_n A \leq 0.07$. A broader comparison with data outside the validity range, captured from Saitoh et al. [16], Ning et al. [18] as well as Moradi et al. [36], has also been conducted. Across this set, the root-mean-square error, defined as $\bar{S} = \sqrt{\frac{\sum_{j=1}^{M}\left[\left(\frac{H_g}{H}\right)_j^{\text{fit}} - \left(\frac{H_g}{H}\right)_j^{\text{data}}\right]^2}{\sum_{j=1}^{M}\left[\left(\frac{H_g}{H}\right)_j^{\text{data}}\right]^2}}$, is approximately $20\%$. Here, $M = 45$ denotes the number of data points involved in this fitting. $\left(\frac{H_g}{H}\right)_j^{\text{fit}}$ and $\left(\frac{H_g}{H}\right)_j^{\text{data}}$ represent the results by the empirical formula and the experimental or numerical simulations, respectively.

In summary, we expect that the corrected fitted expression Eq. (37) can be applied with confidence for large water depth (e.g., $kh \geq \pi$), small wave steepness (e.g., $kA < 0.1$) and large beam-to-gap ratio (e.g., $B/B_g > 41$). It is also expected that if more numerical or experimental results, with broader ranges of water depth ratio, beam-to-gap ratio and wave steepness, are considered in the least-square fitting process, the prediction by the presented empirical formula will also be applicable for a larger regime of these key parameters.

#### 6.3.4 Engineering relevance and future perspectives

In practical offshore operations, accurate prediction of fluid resonance in the narrow gap between vessels is essential for assessing relative motions, evaluating loads on the fastening system and liquid-transfer hoses, and defining safe environmental operating windows. However, high-fidelity CFD simulations or extensive physical model tests that quantify these effects can be computationally expensive and time-consuming, especially when exploring a broad range of wave conditions or vessel loading states.

The empirical correlation developed in this work offers a computationally efficient alternative by providing rapid estimates of resonant amplitudes using only two primary non-dimensional parameters: wave steepness ($kA$) and draft-to-beam ratio ($d/B$). This enables fast screening analyses to identify combinations of environmental and geometric conditions that are more susceptible to strong gap resonance, thereby narrowing the parameter space for subsequent detailed simulations. Such early filtering is particularly valuable during concept selection and preliminary layout design stages, where numerous configurations and loading scenarios must be evaluated.

Furthermore, the explicit form of the empirical correlation make it suitable for embedding into lightweight engineering tools or spreadsheet-based calculators used in industry. It can serve as an inexpensive module within broader offloading assessment frameworks or time-domain simulation environments, reducing the need for repeated CFD campaigns during iterative design processes.

According to the previous studies on 3D gap resonances [23, 29, 70–78], in beam-sea waves, resonant free-surface responses in the gap contain two primary contributions: standing waves due to first-mode response and a spatial mean shift due to end effects. The elevation profile along the gap is always symmetric to the gap center under beam-sea conditions, with the maximum resonant gap response occurring at the gap midpoint due to the dominating modal-type response at resonance. Moreover, in head seas, the response profiles exhibit clearly propagating wave behavior instead of standing waves, attributed to the boundary conditions at the open ends of the gap. Clear asymmetric behavior appears as a consequence of wave–structure interaction, with a much higher value of the most critical resonant gap response obtained close to the bow than at the gap midpoint.

To develop a similar empirical formula for 3D gap resonances, similar procedures as presented in this study can be followed, where the length-to-beam ratio must be introduced as another key non-dimensional parameter. Correspondingly, 3D simulations covering interested ranges of non-dimensional parameters must also be performed. Machine learning technique may be used to collect the numerical dataset and carry out the multi-parameter fitting with the assistance of physical models regarding 3D gap resonances. The modified formulation can be applied to predict the resonant amplitudes of free-surface elevation along the gap under beam-sea wave conditions, especially at the gap midpoint where critical responses are pursued. However, in head seas, additional parameters, e.g. wave directions, Froude or Reynolds numbers, are needed to achieve a satisfactory prediction of resonant gap responses. Following this procedure, the formulation could also help in establishing scaling guidelines for converting model-scale resonance behaviour to full-scale predictions.

To summarize, by linking the derived numerical trends with their practical implications, the empirical model proposed here provides not only improved physical insight into piston-mode gap resonance but also a tangible engineering tool that supports efficient and cost-effective decision-making in the design and operation of side-by-side offshore systems.

## 7 Conclusions

A dimensional analysis is conducted to identify the key parameters related to piston-mode resonances in the narrow gap between two identical, fixed and SBS barges with same drafts. A 2D fully nonlinear NWT is established using CFD to obtain the natural frequency through free-decay tests of the flow motion of the water column within the gap. Thirteen barge drafts and five values of wave steepness are considered to study the combined effects of the draft-to-beam ratio and wave steepness on the fluid response in the gap at resonance. By utilizing a simple massless-damping-lid (MDL) model and results obtained by the numerical model, an empirical expression is proposed to predict the variation of resonant gap response with draft-to-beam ratio and wave steepness. Furthermore, the empirical formula is modified to partially account for the effect of water depth and validated against the experimental and other numerical results. Through this study, some conclusions can be drawn:

- Six non-dimensional parameters are identified relevant to the 2D piston-mode gap resonance problem, four of which (wavelength-to-beam ratio $kB$, gap-to-beam ratio $B_g/B$, draft-to-beam ratio $d/B$ and wave steepness $kA$) are considered in the present study under the wave-only condition at infinite water depth. According to the analytical solution of the natural frequency as well as the potential flow wave theory, $kB$ is primarily dependent on $B_g/B$ and $d/B$. Moreover, under the assumption of a small $B_g/B$, $d/B$ and $kA$ are the two primary factors dominating this hydrodynamic interaction.
- Through free-decay tests, the natural frequency increases first with $B/B_g$, before stabilizing at larger $B/B_g$. However, a reversed trend is observed for its variation with $d/B$, showing a monotonic decrease with $d/B$.
- Regarding the gap response at resonance, the growing $d/B$ results in the increasing resonant response for all values of $k_nA$ considered in the present study, and then it remains constant after a certain $d/B$ value. On the other hand, the resonant wave amplitude in the gap exhibits a nonlinear decrease with $k_nA$ for all the considered $d/B$. It can be explained by the functions of damping and excitation force during resonance through the MDL model, which provides theoretical foundation to suggest an empirical fitting equation.
- In the fitting equation to predict the resonant response in the gap, an inverse proportion to $\sqrt{k_nA}$ is expected for the $k_nA$-related term while the rest terms are assumed as polynomials of $d/B$ according to the MDL model. The ratio of quadratic damping to linear damping are dependent on both $d/B$ and $k_nA$, with a more dominant contribution of quadratic damping over linear damping under larger $d/B$ and $k_nA$.

- To include the water-depth effect $k_n h$, a simplified correction of the fitting formula is carried out based on linear wave theory. The modified formula predicts the resonant gap responses well with satisfactory coincidence to the numerical CFD results when the water depth gets larger.
- By comparison with the results from experiments and other numerical simulations, the modified formula gives reasonable predictions in the resonant gap response under the conditions of negligible gap widths, sufficiently deep water, and small wave steepness.

In summary, the present study provides a clarified understanding of the dominant non-dimensional parameters governing piston-mode gap resonance and the first systematic analysis of the coupled influences of wave steepness and draft-to-beam ratio on the natural frequency and resonant response of water column confined in the gap. This work also proposes a practical two-parameter empirical formulation and its water-depth-corrected extension for prediction of resonant amplitudes, accompanied by satisfactory validation against experimental and numerical data. The present results are also extrapolatable regardless of the actual dimensions of the structures.

In addition to the above scientific findings, the results of this work hold several practical implications for engineering analysis and offshore design. The proposed two-parameter empirical relation provides a computationally inexpensive means to approximate resonant gap responses without resorting to high-fidelity CFD simulations, which are often prohibitively time-consuming during early-stage design of side-by-side offloading systems. These can also serve as a rapid screening tool to identify combinations of wave conditions and loading draughts likely to trigger strong piston-mode resonance, efficiently narrowing the parameter space before performing more detailed hydrodynamic simulations or model tests. Moreover, the empirical formulation can be readily embedded into pre-design tools, e.g., spreadsheet-based calculators or lightweight numerical modules used within concept-selection workflows, to provide quick estimates of gap response envelopes for operability assessment, hose load prediction, or preliminary layout evaluation. The simplicity of the scaling allows it to be integrated into system-level simulators or time-domain offloading analysis frameworks where repeated evaluation of gap resonance would otherwise be too costly. With additional calibration covering broader parameter ranges and potential extension to three-dimensional configurations, the model may also contribute to scaling guidelines used to map model-scale experiments to full-scale conditions while maintaining consistency in the dominant hydrodynamic mechanisms.

Overall, the empirical correlation developed in this study not only enhance the physical understanding of piston-mode gap resonance but also offer an efficient predictive tool that can support preliminary design and feasibility assessments for offshore side-by-side operations. Further dedicated studies are pursued to improve the accuracy within the considered regimes of the key parameters. It is also expected that more key factors, such as Froude and Reynolds numbers, can be taken into account to enlarge the applicability of the fitting formula and possibly extend the formulation to 3D gap resonance problems.



**Acknowledgements**

The authors acknowledge all that provide any contribution to this work.

**Author contribution statement**

**Yunfeng Ding**: Methodology, Software, Data curation, Validation, Investigation, Visualization, Formal Analysis, Writing – original draft, Funding acquisition. **Qicai Niu**: Methodology, Software, Data curation, Validation, Investigation, Visualization, Formal Analysis, Writing – original draft. **Jens Honoré Walther**: Conceptualization, Methodology, Resources, Software, Writing – review & editing, Supervision, Funding acquisition, Project administration. **Hua-Dong Yao**: Resources, Software, Writing – review & editing, Funding acquisition, Project administration. **Yanlin Shao**: Conceptualization, Methodology, Resources, Writing – review & editing, Supervision, Funding acquisition, Project administration. All the authors have approved the final manuscript.

**Data availability**

The data that support the findings of this study is available from the corresponding author upon reasonable request.

**Declaration of competing interest**

All the contributing authors report no conflicts of interest in this work.

**Funding**

This work is supported by the project “Green Transition of the Blue Denmark through Digitalization, Decarbonization, and Safety (SLGreen)” funded by the Innovation Fund Denmark (IFD), the Danish Maritime Fund (DMF), and the Lauritzen Foundation (LF), and the project “Enhancing Shared Mooring System Design for Floating Offshore Wind Farms (ESOMOOR)” funded by the Swedish Energy Agency (SWEA), Innovation Fund Denmark (IFD) and co-funded by the European Union [project reference CETP-2023-00145].

**Use of AI statement**

None.

**Appendix A Mesh Convergence for Empty Tank**

Three mesh resolutions within the free surface refinement zone, including coarse, medium, and fine meshes, are employed in the spatial convergence study. The mesh configurations are listed in Table A1, where $\Delta x$ and $\Delta z$ are the cell sizes in the horizontal and vertical directions, respectively. As mentioned in Section 3, $\Delta z$ is kept constant so that 20 meshes per wave height are maintained while $\Delta x$ varies to achieve different mesh resolutions. The incident wave with $k_n A = 0.02$, which combines with $d/B = 0.98$ to yield the largest resonant gap response in Fig. 7 among all the adopted wave steepness, is considered here as an example. It has to be noted that all the other wave incidences are carefully verified whereas the details are not shown here due to space limits.

**Table A1** Details of the coarse, medium, and fine mesh configurations for free surface refinement. Here, $\lambda$ denotes the incident wavelength and $H$ represents the incident wave height.

| Mesh resolution ($\Delta x/\Delta z$) | No. of cells | $\lambda/\Delta x$ | $H/\Delta z$ |
|---|---|---|---|
| Coarse (8) | 314,600 | 406 | 20 |
| Medium (4) | 522,600 | 813 | 20 |
| Fine (2) | 917,800 | 1,625 | 20 |

Figure A1 presents the time histories of normalized wave elevation $\tilde{\eta} = \eta_i/A$ in the middle of the NWT ($x = 0$) (also the center of the gap with the presence of barges) for three mesh resolutions. The solution based on the fifth-order Stokes wave theory is also included for comparison. The periodic results for five consistent wave periods from $12T$ to $16T$ are selected. It can be observed that the wave elevation is insensitive to the mesh resolution, and the results for all three mesh resolutions coincide well with the theoretical solution. The relative differences of the normalized time-averaged wave amplitude $\tilde{\eta}_a = \eta_a/A$, compared to the theoretical solution, are only $-0.90\%$, $-0.76\%$ and $-0.81\%$ for the coarse, medium and fine resolutions, respectively (See also the summary in Table A2). Therefore, the medium mesh configuration for the free-surface refinement is applied in all the following simulations regarding the wave-barge dynamic system to generate the qualified waves.

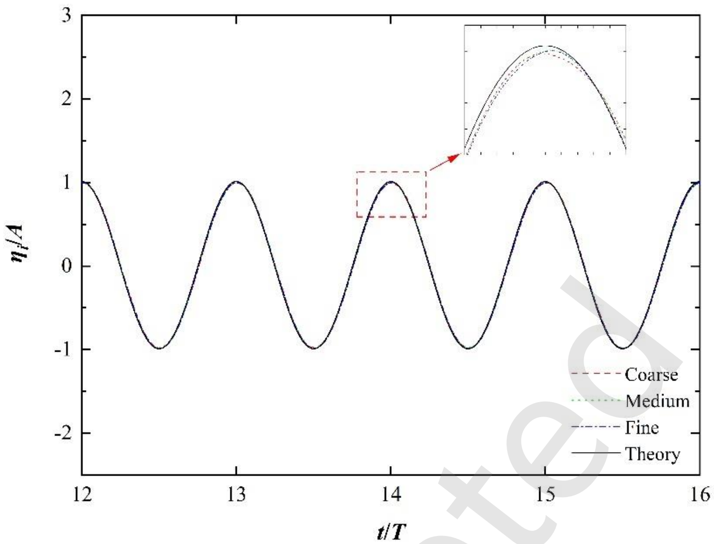


**Figure A1** Normalized wave elevation $\tilde{\eta} = \eta_i/A$ at $x = 0$ for three mesh resolutions of free surface refinement. $T$ denotes the incident wave period and $A$ denotes the incident wave amplitude.

**Table A2** Relative difference $E(\%)$ of the normalized time-averaged wave amplitude $\tilde{\eta}_a = \eta_a/A$ to the theoretical solution at $x = 0$ of three mesh resolutions for free surface refinement.

| Mesh resolution ($\Delta x/\Delta z$) | $E(\%)$ |
|---|---|
| Coarse (8) | $-0.90$ |
| Medium (4) | $-0.76$ |
| Fine (2) | $-0.81$ |

## Appendix B Mesh Convergence for Wave-barge System

The spatial convergence study is further carried out with barges in the NWT using three resolutions of refined meshes in the gap, close to the barge corners and the region around the barges. The meshes in the free surface refinement remain unchanged as the medium configuration in Appendix A. Similarly, a coarse mesh, a medium mesh and a fine mesh are employed, the configurations of which are listed in Table B1. Here, $\Delta g_x$ and $\Delta g_z$ represent the mesh sizes within the gap in the horizontal $x$- and vertical $z$-directions, respectively. The same representation works for those near the barge corners ($\Delta s_x$ and $\Delta s_z$) and the region around the barges ($\Delta v_x$ and $\Delta v_z$). The same incident wave and draft-to-beam ratio of the barges as the empty-tank verification, $k_n A = 0.02$ and $d/B = 0.98$, are applied. The beam-to-gap ratio is set up as $B/B_g = 41$ based on our discussion in Section 6.1.1.

**Table B1** Details of the coarse, medium, and fine configurations of mesh refinement in the gap, near the barge corners and the region around the barges. Here, $\Delta g_j$ ($j = x, z$) represents the mesh sizes within the gap in the horizontal $x$- and vertical $z$-directions, respectively. The same representation works for the meshes near the barge corners $\Delta s_j$ and in the region around the barges $\Delta v_j$.

| Mesh resolution | No. of cells | $\Delta g_x/\Delta x$ | $\Delta g_z/\Delta z$ | $\Delta s_x/\Delta x$ | $\Delta s_z/\Delta z$ | $\Delta v_x/\Delta x$ | $\Delta v_z/\Delta z$ |
|---|---|---|---|---|---|---|---|
| Coarse | 737,872 | 0.375 | 1.5 | 0.75 | 3.0 | 1.5 | 6.0 |
| Medium | 1,296,592 | 0.25 | 1.0 | 0.5 | 2.0 | 1.0 | 4.0 |
| Fine | 3,501,544 | 0.15 | 0.6 | 0.3 | 1.2 | 0.6 | 2.4 |

Figure B1 presents the time histories of normalized wave elevations $\tilde{\eta}_g = \eta_g/A$ in the gap between two barges under the incident wave for the three mesh resolutions. A steady state of four wave periods, $32T$-$36T$, is selected for comparison. As shown in the figure, the free-surface elevations in the gap are close for the three considered mesh resolutions. Compared to the fine mesh, the relative differences of normalized time-averaged amplitudes of gap responses $\tilde{\eta}_{ga} = \eta_{ga}/A$ for the coarse and medium mesh resolutions are only $+2.31\%$ and $-1.11\%$, respectively, as listed in Table B2. To summarize, the medium mesh configuration is used to refine the barges and the gap in between for all the later simulations of the dynamic wave-barge system.

This is a Just Accepted version, keep updated with https://doi.org/10.26599/OCEAN.2026.9470018
*OCEAN* **2026, 2, 9470018**

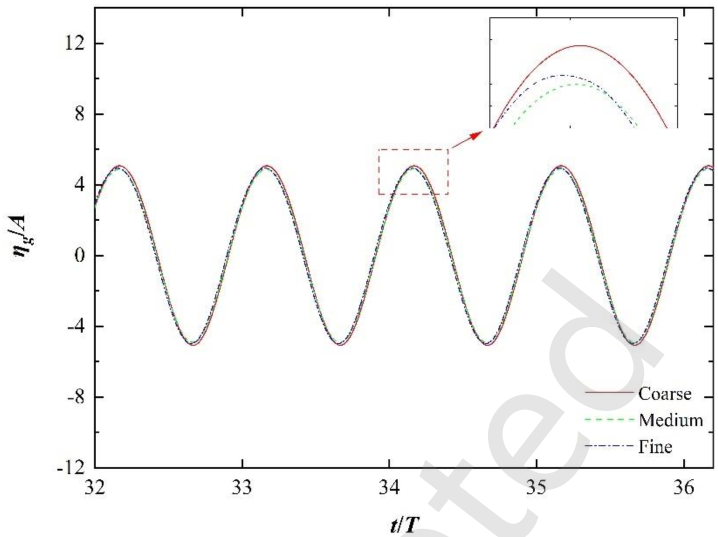


**Figure B1** Normalized wave elevation $\tilde{\eta}_g = \eta_g/A$ in the gap for three resolutions of mesh refinement within the gap, near the barge corners and the region around the barges.

**Table B2** Relative difference $E(\%)$ of the normalized time-averaged wave amplitude $\tilde{\eta}_{ga} = \eta_{ga}/A$ in the gap for three resolutions of mesh refinement to the fine mesh resolution.

| Mesh resolution | $E(\%)$ |
|---|---|
| Coarse | $+2.31$ |
| Medium | $-1.11$ |
| Fine | $0$ |

## Appendix C Validation of the Numerical Free-decay Model

A similar NWT to the physical experiments in Saitoh et al. [16] is established with the same configuration of barge models. In the present numerical free-decay model, an initial released position of the gap fluid is achieved by user-defined functions for volume fractions of air and water phases, similar to that applied in Ding et al. [48], and the natural frequency can be estimated by performing Fast Fourier Transform (FFT) on the free-decay curve of wave elevation in the gap. Three barge drafts and four gap widths are tested, and the normalized natural frequencies are displayed in Fig. C1, together with the experimental measurements. As displayed, the obtained results coincide well with the experimental data, except for cases with large drafts and small gap widths. However, the largest relative discrepancy is only $+4.12\%$ at $B/B_g = 51.0$ and $d/h = 0.50$, as listed in Table C1. In general, the numerical free-decay model is qualified to predict the piston-mode frequency of the flow motion in the gap when resonance occurs.

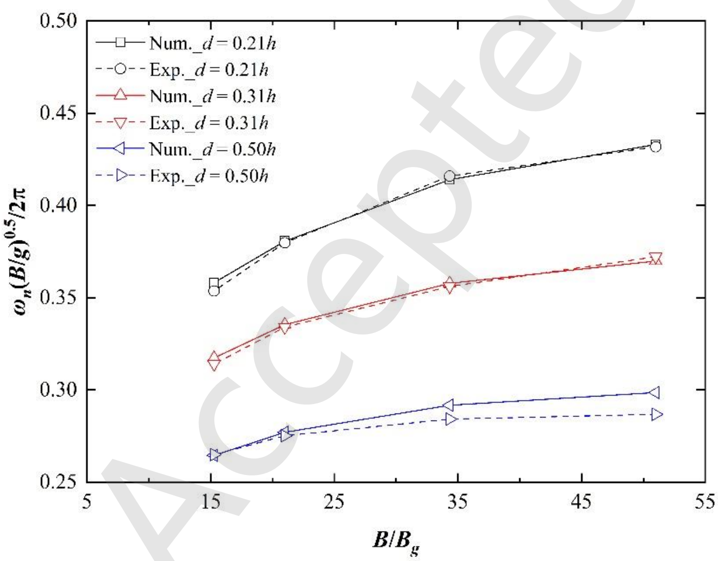


**Figure C1** Non-dimensional natural frequencies of the flow motion of the water column in the gap between two identical, fixed and SBS barges with an equal draft $d$. Here, $\omega_n$ denotes the natural frequency. $B$ and $B_g$ are the characteristic beam length and gap width of this configuration of barge system, respectively. The solid and dashed lines represent the results from the numerical free-decay tests and the physical experiments, respectively.

**Table C1** Relative difference $E(\%)$ of the numerically determined non-dimensional natural frequencies of the flow motion of the water column in the gap, in comparison to experiments.

| $B/B_g$ | $d/h = 0.21$ | $d/h = 0.31$ | $d/h = 0.50$ |
|---|---|---|---|

| | | | |
|---|---|---|---|
| 15.3 | +1.27 | +1.07 | −0.16 |
| 21.0 | +0.23 | +0.40 | +0.67 |
| 34.3 | −0.47 | +0.48 | +2.64 |
| 51.0 | +0.29 | −0.61 | +4.12 |

## Appendix D Validation on Gap Natural Frequency

The ability of the NWT to capture the natural frequency of the flow motion of the water column within the gap is validated against the above-validated free-decay model. The NWT setup is kept consistent with that in Ding et al. [47]. A constant wave steepness $kA = 0.035$ is maintained. Nine incident wave frequencies are tested and the time-averaged non-dimensional amplitudes of wave elevation in the gap are obtained. As demonstrated in Fig. D1, the amplitude reaches the peak at $\varpi_n = 0.277$. The corresponding frequency obtained by the free-decay model $\varpi_{fd}$ is also included in the figure, which coincides with $\varpi_n$. To summarize, the established NWT is reliable in predicting the natural frequency of this dynamic system under wave conditions.

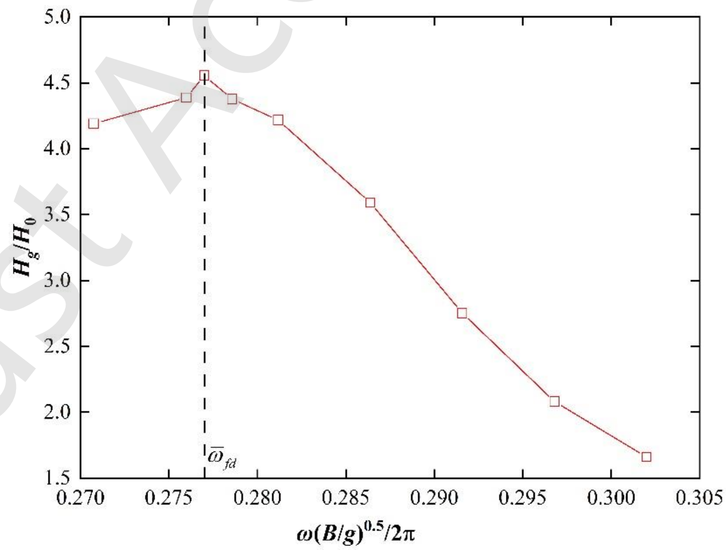


**Figure D1** Normalized wave height in the gap $H_g/H_0$ with a range of incident wave frequencies. Here, $H_g$ represents the crest-to-trough wave height in the gap and $H_0$ represents the incident wave height. $\omega$ is the incident wave frequency. The black dashed line represents the natural frequency $\overline{\omega}_{fd}$ derived by the numerical free-decay model.

**Appendix E Reynolds Number Effect on Resonant Gap Responses**

We define the Reynolds number as $\mathrm{Re} = \frac{|\dot{\eta}_g| d}{\nu}$, where $|\dot{\eta}_g| = \frac{\omega_n H_g}{2}$ denotes the velocity amplitude of time-harmonic resonant gap responses and $\nu$ represents the kinematic viscosity of water. Different definitions of Re may be followed, but it will not influence the conclusions. As an example, the incident wave with $k_n A = 0.02$, interacts with the barge-gap system at $\frac{d}{B} = 0.98$ to yield the largest non-dimensional resonant gap response in Fig. 7 among all the considered conditions, is selected as an example. Five Re values, ranging from $6.7 \times 10^4$ to $1.0 \times 10^7$, are considered, and the non-dimensional resonant amplitudes of the free-surface elevation within the gap are monitored. As observed in Fig. E1, the resonant gap response shows a monotonic increase with Re within the considered Re range. When $\mathrm{Re} \leq 1.0 \times 10^6$, the response is sensitive to Re. After that, the response rises slowly with Re. As discussed, the Re value indeed has a significant effect on the gap response at resonance. A roughly 33.7% difference of response amplitudes between the minimum and maximum Re values is observed. However, the numerical result presented in the paper under $k_n A = 0.02$ and $\frac{d}{B} = 0.98$ is obtained at a model scale with the barge draft of 2 m, and thus a Reynolds number $\mathrm{Re} = 9.4 \times 10^5$. When Froude scaling to a full-scale case with a ship draft of, for instance 12.5 m, the Re value at full scale will be $9.4 \times 10^5 \times (\frac{12.5}{2})^{1.5} = 1.5 \times 10^7$ for this case. It falls within the regime where the resonant response in the gap is less sensitive to the Re value, with an error of nearly 7.2%, indicating a dominant flow separation effect. Therefore, the Re effect on the resonant gap response is little for the cases considered in this study when scaling to the realistic scenario of marine operations.

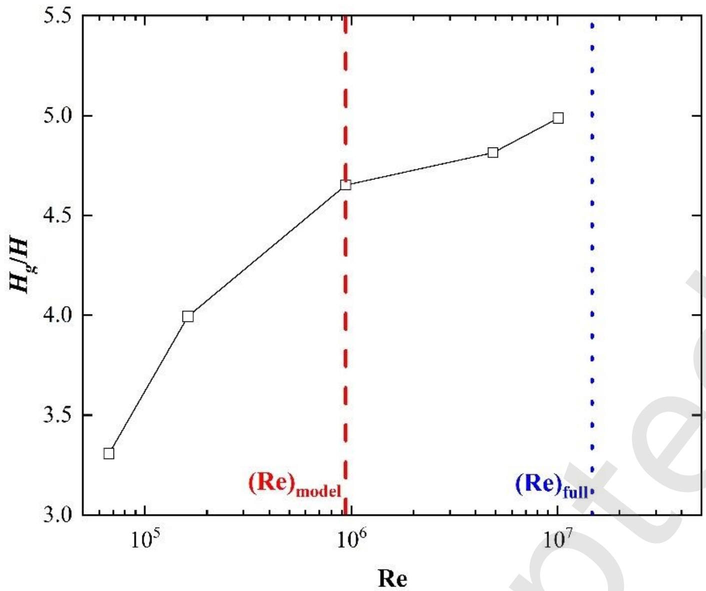


**Figure E1** Non-dimensional resonant gap responses $\frac{H_g}{H}$ with $\frac{d}{B} = 0.98$ under the incident wave with $k_n A = 0.02$. Re is the Reynolds number. $H$ is the incident wave height and $A = \frac{H}{2}$ is the wave amplitude. The red dashed line denotes the Reynolds number in model scale with $(\mathrm{Re})_{\mathrm{model}} = 9.4 \times 10^5$ and the blue dotted line represents the Reynolds number in model scale with $(\mathrm{Re})_{\mathrm{full}} = 1.5 \times 10^7$.

## References

[1] Zhao, W. H., Milne, I. A., Efthymiou, M., Wolgamot, H. A., Draper, S., Taylor, P. H., Taylor, R. E. (2018). Current practice and research directions in hydrodynamics for FLNG-side-by-side offloading. *Ocean Engineering*, 158: 99–110. https://doi.org/10.1016/j.oceaneng.2018.03.076.

[2] Bellezi, C. A., Cheng, L. Y., Arai, M. (2017). Analysis of the effect of the hull shape on piston-like resonant flow in narrow gap: Nonlinear numerical analysis by a fully Lagrangian particle method. In Conference Proceedings of the Japan Society of Naval Architects and Ocean Engineers, The Japan Society of Naval Architects and Ocean Engineers, p 85–89.

[3] Miao, G. P., Ishida, H., Saitoh, T. (2000). Influence of gaps between multiple floating bodies on wave forces. *China Ocean Engineering*, 15(4): 407–422.

[4] Molin, B. (2001). On the piston and sloshing modes in moonpools. *Journal of Fluid Mechanics*, 430: 27–50. https://doi.org/10.1017/S0022112000002871.

[5] Iwata, H., Saitoh, T., Miao, G. P. (2007). Fluid resonance in narrow gaps of very large floating structure composed of rectangular modules. In Proceedings of the Fourth International Conference on Asian and Pacific Coasts, Nanjing, China, p 815–826.

[6] Faltinsen, O. M., Rognebakke, O. F., Timokha, A. N. (2007). Two-dimensional resonant piston-like sloshing in a moonpool. *Journal of Fluid Mechanics*, 575: 359–397. https://doi.org/10.1017/S002211200600440X.

[7] Zhu, H. R., Zhu, R. C., Miao, G. P. (2008). A time domain investigation on the hydrodynamic resonance phenomena of 3-D multiple floating structures. *Journal of Hydrodynamics*, 20: 611–616. https://doi.org/10.1016/S1001-6058(08)60102-X.

[8] Molin, B., Zhang, X., Huang, H., Remy, F. (2018). On natural modes in moonpools and gaps in finite depth. *Journal of Fluid Mechanics*, 840: 530–554. https://doi.org/10.1017/jfm.2018.69.

[9] Kristiansen, T., Faltinsen, O.M. (2008). Application of a vortex tracking method to the piston-like behaviour in a semi-entrained vertical gap. *Applied Ocean Research*, 30(1): 1–16. https://doi.org/10.1016/j.apor.2008.02.003.

[10] Kristiansen, T., Faltinsen, O.M. (2010). A two-dimensional numerical and experimental study of resonant coupled ship and piston-mode motion. *Applied Ocean Research*, 32(2): 158–176. https://doi.org/10.1016/j.apor.2009.10.001.

[11] Faltinsen, O. M., Firoozkoohi, R., Timokha, A. N. (2011). Steady-state liquid sloshing in a rectangular tank with a slat-type screen in the middle: Quasilinear modal analysis and experiments.

*Physics of Fluids*, 23(4): 042101. https://doi.org/10.1063/1.3562310.

[12] Liu, C. Y., Lu, L., Tan, L., Song, Z., Zhou, Z. (2016). Experimental and numerical investigations of wave resonance in gap between two floating barges with various breadths. In Proceedings of the 8th Chinese-German Joint Symp. Hydraul. Ocean Eng., Qingdao, China.

[13] Tan, L., Lu, L., Tang, G. Q., Cheng, L., Chen, X. B. (2019). A viscous damping model for piston mode resonance. *Journal of Fluid Mechanics*, 871: 510–533. https://doi.org/10.1017/jfm.2019.302.

[14] Milne, I. A., Kimmoun, O., Graham, J. M. R., Molin, B. (2022). An experimental and numerical study of the resonant flow between a hull and a wall. *Journal of Fluid Mechanics*, 930: A25. https://doi.org/10.1017/jfm.2021.877.

[15] Wang, X. Y., Liu, Y., Meringolo, D. D., Lu, L. (2023). Experimental study on the wave-induced fluid resonance and suppression scheme in the narrow gap of two floating rectangular structures. *Physics of Fluids*, 35(12): 127119. https://doi.org/10.1063/5.0180297.

[16] Saitoh, T., Miao, G. P., Ishida, H. (2006). Theoretical analysis on appearance condition of fluid resonance in a narrow gap between two modules of very large floating structure. In Proceedings of the 3rd Asia-Pacific Workshop on Marine Hydrodynamics, Shanghai, China, p 170–175.

[17] Tan, L., Lu, L., Liu, Y., Sabodas, O. A., Teng, B. (2014). Dissipative effects of resonant waves in confined space formed by floating box in front of vertical wall. In the 11th ISOPE Pacific/Asia Offshore Mechanics Symposium, Shanghai, China, ISOPE-P-14-080.

[18] Ning, D. Z., Zhu, Y., Zhang, C. W., Zhao, M. (2018). Experimental and numerical study on wave response at the gap between two barges of different draughts. *Applied Ocean Research*, 77: 14–25. https://doi.org/10.1016/j.apor.2018.05.010.

[19] Faltinsen, O. M., Timokha, A. N. (2015). On damping of two-dimensional piston-mode sloshing in a rectangular moonpool under forced heave motions. *Journal of Fluid Mechanics*, 772: R1. https://doi.org/10.1017/jfm.2015.234.

[20] Ning, D. Z., Su, X. J., Zhao, M., Teng, B. (2015). Hydrodynamic difference of rectangular-box systems with and without narrow gaps. *Journal of Engineering Mechanics*, 141(8): 04015023. https://doi.org/10.1061/(ASCE)EM.1943-7889.0000935.

[21] Ning, D. Z., Su, X. J., Zhao, M., Teng, B. (2015). Numerical study of resonance induced by wave action on multiple rectangular boxes with narrow gaps. *Acta Oceanologica Sinica*, 34(5): 92–102. https://doi.org/10.1007/s13131-015-0672-1.

[22] Tan, L., Tang, G. Q., Zhou, Z. B., Cheng, L., Chen, X. B., Lu, L. (2017). Theoretical and numerical investigations of wave resonance between two floating bodies in close proximity. *Journal of Hydrodynamics*, 29(5): 805–816. https://doi.org/10.1016/S1001-6058(16)60792-8.

[23] Zhao, W. H., Pan, Z. Y., Lin, F., Li, B. B., Taylor, P. H., Efthymiou, M. (2018). Estimation of gap resonance relevant to side-by-side offloading. *Ocean Engineering*, 153: 1–9. https://doi.org/10.1016/j.oceaneng.2018.01.056.

[24] Lu, L., Tan, L., Zhou, Z. B., Zhao, M., Ikoma, T. (2020). Two-dimensional numerical study of gap resonance coupling with motions of floating body moored close to a bottom-mounted wall. *Physics of Fluids*, 32(9): 092101. https://doi.org/10.1063/5.0017947.

[25] Tan, L., Cheng, L., Ikoma, T. (2021). Damping of piston mode resonance between two fixed boxes. *Physics of Fluids*, 33(6): 062117. https://doi.org/10.1063/5.0053507.

[26] Song, Z. W., Lu, L., Cheng, L., Liu, Y., Tang, G. Q., Lou, X. F. (2022). Fully nonlinear numerical investigations on the dynamics of fluid resonance between multiple bodies in close proximity. *Physics of Fluids*, 34(12): 122106. https://doi.org/10.1063/5.0124470.

[27] Zou, M. Y., Chen, M. S., Zhu, L., Li, L., Zhao, W. H. (2023). A constant parameter time domain model for dynamic modelling of multi-body system with strong hydrodynamic interactions. *Ocean Engineering*, 268: 113376. https://doi.org/10.1016/j.oceaneng.2022.113376.

[28] Lu, L., Teng, B., Sun, L., Chen, B. (2011). Modelling of multi-bodies in close proximity under water waves—Fluid forces on floating bodies. *Ocean Engineering*, 38(13): 1403–1416. https://doi.org/10.1016/j.oceaneng.2011.06.008.

[29] Chua, K. H., Taylor, R. E., Choo, Y. S. (2018). Hydrodynamic interaction of side-by-side floating bodies part I: Development of CFD-based numerical analysis framework and modified potential flow model. *Ocean Engineering*, 166: 404–415. https://doi.org/10.1016/j.oceaneng.2017.06.031.

[30] Jiang, S. C., Bai, W., Tang, G. Q. (2018). Numerical simulation of wave resonance in the narrow gap between two non-identical boxes. *Ocean Engineering*, 156: 38–60. https://doi.org/10.1016/j.oceaneng.2018.02.055.

[31] Jiang, S. C., Bai, W., Cong, P. W., Yan, B. (2019). Numerical investigation of wave forces on two side-by-side non-identical boxes in close proximity under wave actions. *Marine Structures*, 63: 16–44. https://doi.org/10.1016/j.marstruc.2018.08.007.

[32] Jiang, S. C., Bai, W., Tang, G. Q. (2019). Numerical investigation of piston-modal wave resonance in the narrow gap formed by a box in front of a wall. *Physics of Fluids*, 31(5): 052105. https://doi.org/10.1063/1.5092657.

[33] Jiang, S. C., Bai, W. (2020). Coupling analysis for sway motion box with internal liquid sloshing under wave actions. *Physics of Fluids*, 32(7): 072106. https://doi.org/10.1063/5.0015058.

[34] Yin, Y., Jiang, S. C., Liu, H. (2023). Fluid resonance in the narrow gap for a ship close to the vertical caisson on impermeable and permeable beds. *Ocean Engineering*, 286: 115422.

https://doi.org/10.1016/j.oceaneng.2023.115422.

[35] Lu, L., Cheng, L., Teng, B., Zhao, M. (2010). Numerical investigation of fluid resonance in two narrow gaps of three identical rectangular structures. *Applied Ocean Research*, 32(2): 177–190. https://doi.org/10.1016/j.apor.2009.10.003.

[36] Moradi, N., Zhou, T. M., Cheng, L. (2016). Two-dimensional numerical study on the effect of water depth on resonance behaviour of the fluid trapped between two side-by-side bodies. *Applied Ocean Research*, 58: 218–231. https://doi.org/10.1016/j.apor.2016.03.018.

[37] Gao, J. L., He, Z. W., Zang, J., Chen, Q., Ding, H. Y., Wang, G. (2019). Topographic effects on wave resonance in the narrow gap between fixed box and vertical wall. *Ocean Engineering*, 180: 97–107. https://doi.org/10.1016/j.oceaneng.2019.03.040.

[38] Gao, J. L., Chen, H. Z., Zang, J., Chen, L. F., Wang, G., Zhu, Y. Z. (2020). Numerical investigations of gap resonance excited by focused transient wave groups. *Ocean Engineering*, 212: 107628. https://doi.org/10.1016/j.oceaneng.2020.107628.

[39] Gao, J. L., He, Z. W., Zang, J., Chen, Q., Ding, H. Y., Wang, G. (2020). Numerical investigations of wave loads on fixed box in front of vertical wall with a narrow gap under wave actions. *Ocean Engineering*, 206: 107323. https://doi.org/10.1016/j.oceaneng.2020.107323.

[40] Gao, J. L., Zang, J., Chen, L. F., Chen, Q., Ding, H. Y., Liu, Y. Y. (2019). On hydrodynamic characteristics of gap resonance between two fixed bodies in close proximity. *Ocean Engineering*, 173: 28–44. https://doi.org/10.1016/j.oceaneng.2018.12.052.

[41] Li, Y. J., Wang, X., K. (2021). Numerical study of effects of gap and incident wave steepness on water resonance between two rectangular barges. *European Journal of Mechanics-B/Fluids*, 86: 157–168. https://doi.org/10.1016/j.euromechflu.2020.12.001.

[42] Ding, Y. F., Walther, J. H., Shao, Y. L. (2024). Effect of wave–current interaction on gap

resonance between side-by-side barges. *Applied Ocean Research,* 150: 104073. https://doi.org/10.1016/j.apor.2024.104073.

[43] Fournier J. R., Mamoun N., Chen X. B. (2006). Hydrodynamics of two side-by-side vessels experiments and numerical simulations. In Proceedings of the Sixteenth International Offshore and Polar Engineering Conference (ISOPE 2006), San Francisco, California, USA, ISOPE-I-06-349.

[44] Molin, B., Remy, F., Camhi, A., Ledoux, A. (2009). Experimental and numerical study of the gap resonances in-between two rectangular barges. In Proceedings of the 13th Congress of the International Maritime Association of the Mediterranean (IMAM 2009), Istanbul, Turkey, p 12–15.

[45] Kimmoun, O., Molin, B., Oikonomidou, H. (2011). Wave drift force on a rectangular barge by a vertical wall. In Proceedings of the 26th International Workshop on Water Waves and Floating Bodies (IWWWFB), Athens, Greece.

[46] Milne, I. A., Kimmoun, O., Molin, B., Graham, J. M. R. (2020). An experimental and numerical study of the vortex shedding dynamics during gap resonance. In Proceedings of the 35th International Workshop on Water Waves and Floating Bodies (IWWWFB), Seoul, South Korea.

[47] Ding, Y. F., Walther, J. H., Shao, Y. L. (2022). Higher-order gap resonance between two identical fixed barges: A study on the effect of water depth. *Physics of Fluids*, 34(5): 052113. https://doi.org/10.1063/5.0089564.

[48] Ding, Y. F., Walther, J. H., Shao, Y. L. (2022). Higher-order gap resonance and heave response of two side-by-side barges under Stokes and cnoidal waves. *Ocean Engineering*, 266: 112835. https://doi.org/10.1016/j.oceaneng.2022.112835.

[49] Buckingham, E. (1914). On physically similar systems; illustrations of the use of dimensional equations. *Physical Review*, 4(4): 345. https://doi.org/10.1103/PhysRev.4.345.

[50] Jacobsen, N. G., Fuhrman, D. R., Fredsøe, J. (2012). A wave generation toolbox for the open-source CFD library: OpenFoam®. *International Journal for Numerical Methods in Fluids*, 70(9): 1073–1088. https://doi.org/10.1002/fld.2726.

[51] Chen, L. F., Zang, J., Hillis, A. J., Morgan, G. C. J., Plummer, A. R. (2014). Numerical investigation of wave–structure interaction using OpenFOAM. *Ocean Engineering*, 88: 91–109. https://doi.org/10.1016/j.oceaneng.2014.06.003.

[52] Kim, J. W., Kyoung, J. H., Bai, K. J., Ertekin, R. C. (2004). A numerical study of nonlinear diffraction loads on floating bodies due to extreme transient waves. In Proceedings of the 25th Symposium on Naval Hydrodynamics, St. John's, Newfoundland and Labrador, Canada.

[53] Kim, J., Jaiman, R., Cosgrove, S., O'Sullivan, J. (2011). Numerical wave tank analysis of wave run-up on a truncated vertical cylinder. In International Conference on Offshore Mechanics and Arctic Engineering, Rotterdam, Netherlands, OMAE2011-50283, p 805-814. https://doi.org/10.1115/OMAE2011-50283.

[54] Kim, J., O'Sullivan, J., Read, A. (2012). Ringing analysis of a vertical cylinder by Euler overlay method. In International Conference on Offshore Mechanics and Arctic Engineering, American Society of Mechanical Engineers, Rio de Janeiro, Brazil, OMAE2012-84091, p 855–866. https://doi.org/10.1115/OMAE2012-84091.

[55] Hirt, C. W., Nichols, B. D. (1981). Volume of fluid (VOF) method for the dynamics of free boundaries. *Journal of Computational Physics*, 39(1): 201–225. https://doi.org/10.1016/0021-9991(81)90145-5.

[56] Siemen (2021). STAR-CCM+ User Guide Version 16.06. Siemens PLM Software Inc., Munich, Germany.

[57] Jackson, D., Launder, B. (2007). Osborne Reynolds and the publication of

his papers on turbulent flow. *Annu. Rev. Fluid Mech.*, 39(1): 19–35. https://doi.org/10.1146/annurev.fluid.39.050905.110241.

[58] Boussinesq, J. (1877). Theorie de l'ecoulement tourbillant. *Mem. Acad. Sci. Inst. Fr. 0368-9263*, 23: 46–50.

[59] Perić, M. (2018). Best practices for wave flow simulations. *The Naval Architect International Journal of the Royal Institute of Naval Architects*, 142: 38–42.

[60] Lien, F. S. (1996). Low-Reynolds-number eddy-viscosity modelling based on non-linear stress-strain/vorticity relations. In Proceedings of the 3rd Symposium on Engineering Turbulence Modelling and Measurements, Crete, Greece, p 1–10.

[61] Hanjalić, K., Launder, B. E. (1972). A Reynolds stress model of turbulence and its application to thin shear flows. *Journal of Fluid Mechanics*, 52(4): 609–638. https://doi.org/10.1017/S002211207200268X.

[62] Spalart, P. R., Rumsey, C. L. (2007). Effective inflow conditions for turbulence models in aerodynamic calculations. *AIAA Journal*, 45(10): 2544–2553. https://doi.org/10.2514/1.29373.

[63] Perić, R., Abdel-Maksoud, M. (2016). Reliable damping of free-surface waves in numerical simulations. *Ship Technology Research*, 63(1): 1–13. https://doi.org/10.1080/09377255.2015.1119921.

[64] Perić, R., Abdel-Maksoud, M. (2018). Analytical prediction of reflection coefficients for wave absorbing layers in flow simulations of regular free-surface waves. *Ocean Engineering*, 147: 132–147. https://doi.org/10.1016/j.oceaneng.2017.10.009.

[65] Ferziger, J. H., Perić, M. (2002). Computational Methods for Fluid Dynamics. Springer Berlin, Heidelberg. https://doi.org/10.1007/978-3-642-56026-2.

[66] Fenton, J. D. (1988). The numerical solution of steady water wave problems. *Computers &*

*Geosciences*, 14(3): 357–368. https://doi.org/10.1016/0098-3004(88)90066-0.

[67] Le Méhauté, B. (1976). An Introduction to Hydrodynamics and Water Waves. Springer Berlin, Heidelberg, p 205. https://doi.org/10.1007/978-3-642-85567-2.

[68] Newman, J. N. (1977). Marine Hydrodynamics. The MIT Press. http://library.oapen.org/handle/20.500.12657/26039.

[69] Lu, L., Cheng, L., Teng, B., Sun, L. (2010). Numerical simulation and comparison of potential flow and viscous fluid models in near trapping of narrow gaps. *Journal of Hydrodynamics*, 22(Suppl 1): 120–125. https://doi.org/10.1016/S1001-6058(09)60180-3.

[70] Ding, Y., Walther, J. H., Liang, H., Shao, Y. (2025). CFD modeling of three-dimensional gap resonances between side-by-side barges under combined wave and current excitation. *Marine Structures*, 103: 103826. https://doi.org/10.1016/j.marstruc.2025.103826.

[71] Zhao, W., Wolgamot, H. A., Taylor, P. H., Taylor, R. E. (2017). Gap resonance and higher harmonics driven by focused transient wave groups. *Journal of Fluid Mechanics*, 812: 905-939. https://doi.org/10.1017/jfm.2016.824.

[72] Liang, H., Chua, K. H., Wang, H. C., Choo, Y. S. (2021). Numerical and experimental investigations into fluid resonance in a gap between two side-by-side vessels. *Applied Ocean Research*, 111: 102581. https://doi.org/10.1016/j.apor.2021.102581.

[73] Chua, K. H., Taylor, R. E., Choo, Y. S. (2018). Hydrodynamic interaction of side-by-side floating bodies, Part II: Applications of modified linear potential flow and numerical analysis framework to fixed barges. *Ocean Engineering*, 164: 465-481. https://doi.org/10.1016/j.oceaneng.2018.06.060.

[74] Chua, K. H., de Mello, P. C., Nishimoto, K., Choo, Y. S. (2019). Model experiments of floating side-by-side barges. In International Conference on Offshore Mechanics and Arctic

Engineering, American Society of Mechanical Engineers, Glasgow, Scotland, UK, OMAE2019-95238, V009T12A008. https://doi.org/10.1115/OMAE2019-95238.

[75] Wang, H., Draper, S., Zhao, W., Wolgamot, H., Cheng, L. (2017). Development of a CFD model to simulate three-dimensional gap resonance applicable to FLNG side-by-side offloading. In International Conference on Offshore Mechanics and Arctic Engineering, American Society of Mechanical Engineers, Trondheim, Norway, OMAE2017-61673, V001T01A032. https://doi.org/10.1115/OMAE2017-61673.

[76] Yang, Y., Zhu, R., Chen, X., Jiang, Y. (2018). Numerical study on fluid resonance of 3-D multi-bodies by a non-reflection numerical wave tank. *Applied Ocean Research*, 80: 166-180. https://doi.org/10.1016/j.apor.2018.09.002.

[77] Zhao, W., Molin, B., Wang, Y., Wolgamot, H. A., Taylor, P. H. (2022). Nonlinear harmonics of gap fluid resonance with floating body motions. *Journal of Fluid Mechanics*, 951: A23. https://doi.org/10.1017/jfm.2022.834.

[78] Zou, M., Chen, M., Zhu, L., Yun, Q., Zhao, W., Liang, Q., Zhao, Y. (2024). Experimental and numerical investigation of gap resonances between side-by-side fixed barges under beam sea excitation. *Ocean Engineering*, 297: 117150. https://doi.org/10.1016/j.oceaneng.2024.117150.